REGIONAL WARMING EVENT IN WINTER ON THE ROSS ICE SHELF, ANTARCTICA AS OBSERVED BY UW-MADISON AUTOMATIC WEATHER STATIONS

by

David E. Mikolajczyk

A thesis submitted in partial fulfillment of

the requirements for the degree of

Master of Science

(Atmospheric and Oceanic Sciences)

at the

UNIVERSITY OF WISCONSIN-MADISON

2022

ABSTRACT

From 12-15 July 2007, a regional warming event in winter (RWEW) on the Ross Ice Shelf (RIS) was observed by the University of Wisconsin-Madison (UW-Madison) Automatic Weather Station (AWS) network. A warming event is defined as an AWS observing an increase in temperature of 30° C or greater in five days or fewer. Preceding this RWEW, a stationary low in the Ross Sea and ridge downstream in the Amundsen Sea built up a pool of warm air just off the coast and northeast of the RIS. Calm conditions over the RIS led to cooling surface temperatures. A strong baroclinic zone stretched along the boundary of the pool of warm air northwest to the stationary low and west towards the Adelie Land Coast. A barotropic cyclonic disturbance progressed from the Adelie Land coast along this baroclinic zone and merged with the stationary cyclone in the Ross Sea, after which it deepened and progressed southward towards the RIS. The approaching cyclone eroded the cold pool and initiated the RWEW with a warm front that brought warm air advection, cloud cover, and increased wind speeds.

Fourteen AWS observed warming events during this RWEW. Due to their spread across the RIS and varying topographical influences, several mechanisms led to the warming events. This thesis investigates how the atmospheric environment evolved throughout the RWEW in the context of known circulation regimes such as the Amundsen Sea Low, the Ross Air Stream, and leeside cyclogenesis off the Adelie Land coast. This thesis also compares AWS observations during the RWEW to their climatological means to investigate the significance of the temperature and wind changes because of this RWEW.

ACKNOWLEDGMENTS

The research for this thesis has been many years in the making. To Linda Keller and Matthew Lazzara of the Antarctic Meteorological Research Center, thank you for introducing me to this research as an undergraduate at the University of Wisconsin-Madison and supporting me at work and throughout my undergraduate and graduate career.

To Jonathan Martin, your undergraduate synoptic meteorology course was my favorite course I've taken. I'm happy that I've had the privilege of having you as my advisor for my Master's research. Thank you for helping me understand and conceptualize the atmosphere, your advice in organizing this research into its final form, and your inspiration in making me a better scientist and person.

To the High Impact Weather Group, thank you for providing an interesting, thought-provoking, and fun environment for learning about everyone's research and for being able to present my own research.

To Steph Henderson and Tristan L'Ecuyer, thank you for your advice and support in the early days of my graduate career, as I was trying to find the correct direction for this research, and in the last days of reading through the final drafts.

To Elin McIlhattan, thank you for making the CloudSat/CALIPSO plots, helping me understand them, and for proofing through the final drafts of this thesis.

To Marian Mateling, thank you for helping me with Python in the early days of this research. It was invaluable to get your help.

To my mom, Cindy, and my dad, Ed, thank you for your endless love and support. I feel so lucky to have such wonderful parents as you.

To my partner, Krissy, thank you for being there for me, whether it was seemingly insignificant (“Look, Krissy! A plot with multiple lines on it!”) or very important (helping me finish the presentation for my defense). I’m so happy I can have you along with me on this journey.

And finally, thank you to all my friends, and to my coworkers and colleagues I’ve met in the Atmospheric and Oceanic Sciences Department and Space Science and Engineering Center over the years. Whether you helped me understand positive vorticity advection by the thermal wind, helped me figure out why I couldn’t remotely log in, or were just a good friend to talk to, you were vital in helping me make this research and this Master’s degree possible.

This work is based on University of Wisconsin-Madison Automatic Weather Station data, with support from the National Science Foundation, grants 1543305 and 1924730.

TABLE OF CONTENTS

LIST OF TABLES

LIST OF FIGURES

A through E at the bottom correspond to a). The time denotes the time the satellites were at the midpoint of the red line in a).

Figure 4.3: Infrared satellite composite image with annotated letters corresponding to locations in Fig. 4.2 and yellow dots denoting AWS locations.

Figure 4.4: As in Fig. 2.1, except blue dots are ERA5 10-m wind speeds (m s^{-1}), and dashed red lines denote the temperature trend before, during, and after each respective warming event.

Figure 4.5: ERA-I 06 UTC 12 July 2007 vertical temperature (° C) profile (solid red line) versus pressure (hPa, note the logarithmic scale) and wind barbs (m s^{-1}) at the grid point nearest Elaine (-83.16°, 174.38°).

Figure 4.6: ERA-I 12 UTC 10 July 2007 mean sea level pressure (hPa) (black contours), 2-m temperature (° C) (dashed red contours, 850-hPa relative vorticity (10^{-4} s^{-1}) (fill contours from -4 to 0 every 0.5), and 10-m wind barbs (m s^{-1}). AWS are plotted as in Fig. 3.1a.

Figure 4.7: As in Fig. 4.6 but for 00 UTC 11 July 2007.

Figure 4.8: As in Fig. 4.1 but for 12-15 July 2007.

Figure 4.9: ERA-I 12 UTC 14 July geopotential height (m) (black contours), temperature (° C) (dashed red contours), relative vorticity (10^{-4} s^{-1}) (fill contours from -4 to 0 every 0.5), and wind barbs (m s^{-1}).

Figure 4.10: ERA5 time versus pressure (hPa, note the logarithmic scale) of temperature (K) (blue contours) at the grid point nearest Elaine. Black vertical lines denote beginning and ending of warming event.

Figure 4.11: As in Fig. 4.5 but for 00 UTC 15 July 2007.

Figure 4.12: As in Fig. 4.2 but for 07:39 UTC 14 July 2007.

Figure 4.13: As in Fig. 4.3 but for 06 UTC 14 July 2007.

ABBREVIATIONS

A-Train	National Aeronautics and Space Administration Afternoon-Train
AMRC	Antarctic Meteorological Research Center
AWS	Automatic Weather Station
BOACRE	Bottom of the Atmosphere Longwave Cloud Radiative Effect
C	Celsius
CALIOP	Cloud Aerosol Lidar with Orthogonal Polarization
CALIPSO	Cloud-Aerosol Lidar and Infrared Pathfinder
CFSR	Climate Forecast System Reanalysis
crl	Carolyn
CPR	Cloud Profiling Radar
dBZ	Reflectivity
DLR	Downwelling Longwave Radiation
DPC	Data Processing Center
ECMWF	European Centre for Medium Range Weather Forecasts
eln	Elaine
ERA5	European Centre for Medium Range Weather Forecasts (ECMWF) Reanalysis Version 5
ERA-I	European Centre for Medium Range Weather Forecasts (ECMWF) Reanalysis Interim
erc	Eric
fer	Ferrell
gil	Gill

hPa	HectoPascals
IR	Infrared
K	Kelvin
km	Kilometer
lda	Linda
let	Lettau
lor	Lorne
lr2	Laurie II
LW	Longwave
m	Meter
MERRA-2	Modern-Era Retrospective Analysis for Research and Applications, Version 2
mln	Marilyn
MM5	Pennsylvania State University-National Center for Atmospheric Research Mesoscale Model
NASA	National Aeronautics and Space Administration
PGF	Pressure Gradient Force
pgn	Pegasus North
q10	10-minute quality-controlled
RWEW	Regional Warming Event in Winter
RAS	Ross Air Stream
RIS	Ross Ice Shelf
s	Seconds
swt	Schwerdtfeger

UTC	Coordinated Universal Time
UW-Madison	University of Wisconsin-Madison
vto	Vito
W	Watts
wdb	Windless Bight

CHAPTER 1: INTRODUCTION

From 12-15 July 2007, a regional warming event in winter (RWEW) was observed on the Ross Ice Shelf (RIS) by the University of Wisconsin-Madison (UW-Madison) Automatic Weather Station (AWS) network. For this study, a warming event is defined as an AWS observing an increase in temperature of greater than 30° C in five or fewer days. To be a regional warming event, more than one AWS needs to observe such a warming event in the same region of Antarctica at approximately the same time. For this RWEW, a warming event was observed by 14 AWSs on the RIS. The warming began at different times at the different AWSs, and for some stations the temperature increase was at different rates, but the event essentially spanned the entire RIS. This study examines how the meteorological environment preceding the RWEW, and subsequent development throughout, led to numerous RIS AWSs observing the warming.

The Antarctic continent is comprised almost entirely of a deep layer of ice and snow and is divided into two broad regions: East Antarctica and West Antarctica (Fig. 1.1a, b). Refer to Fig. 1.1b for regions of the Antarctic referenced in this study. The RIS is a flat, floating ice shelf with elevations near sea level and an area approximately the size of France. It is formed by glacier ice flowing from the East Antarctic Plateau to the west and south and from West Antarctica to the east. The RIS is bordered on its west and south by the relatively steep Transantarctic Mountains; on its east by the gentler-sloping West Antarctic Plateau; and on its north by the Ross Sea.

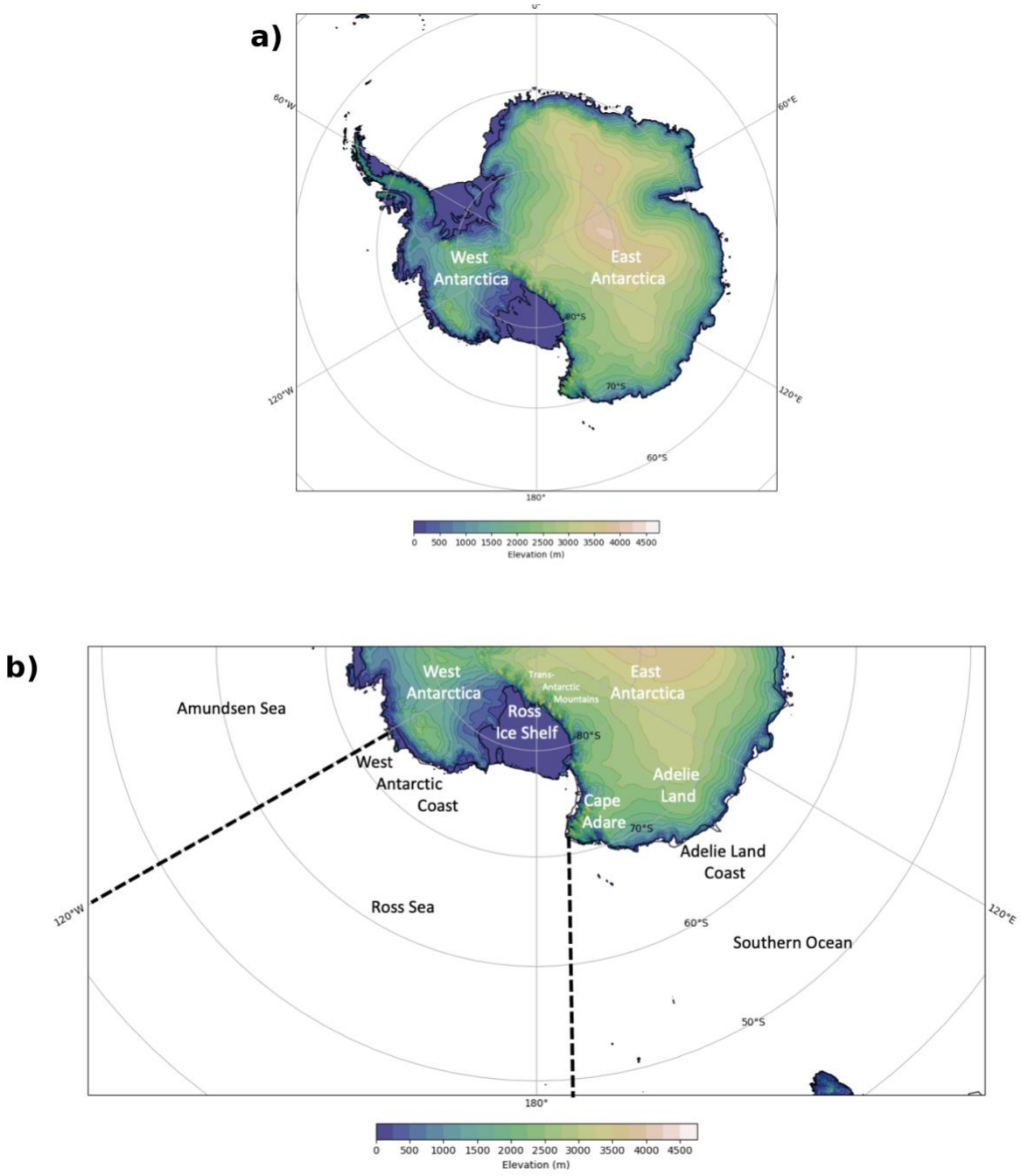

Figure 1.1: a) The topography of Antarctica (m). Contours are every 250 m. b) Labels of regions referenced in this study. The black dashed lines separate the Southern Ocean, Ross Sea, and Amundsen Sea.

The UW-Madison has managed an AWS network in Antarctica since 1980 (Lazzara et al. 2012a). These AWS observe near-surface meteorological variables such as temperature, pressure, and wind speed and direction. Over the years, this AWS network has grown to include upwards of 60 AWS, approximately one-third of which are located throughout the RIS. In 2007, there were 19 AWS on the RIS (Fig. 1.2), with the majority in the northwest portion of the RIS in the Ross Island region. Despite this local concentration of stations, the distribution of the RIS AWS still captures the different influences of topography on temperature and wind regimes.

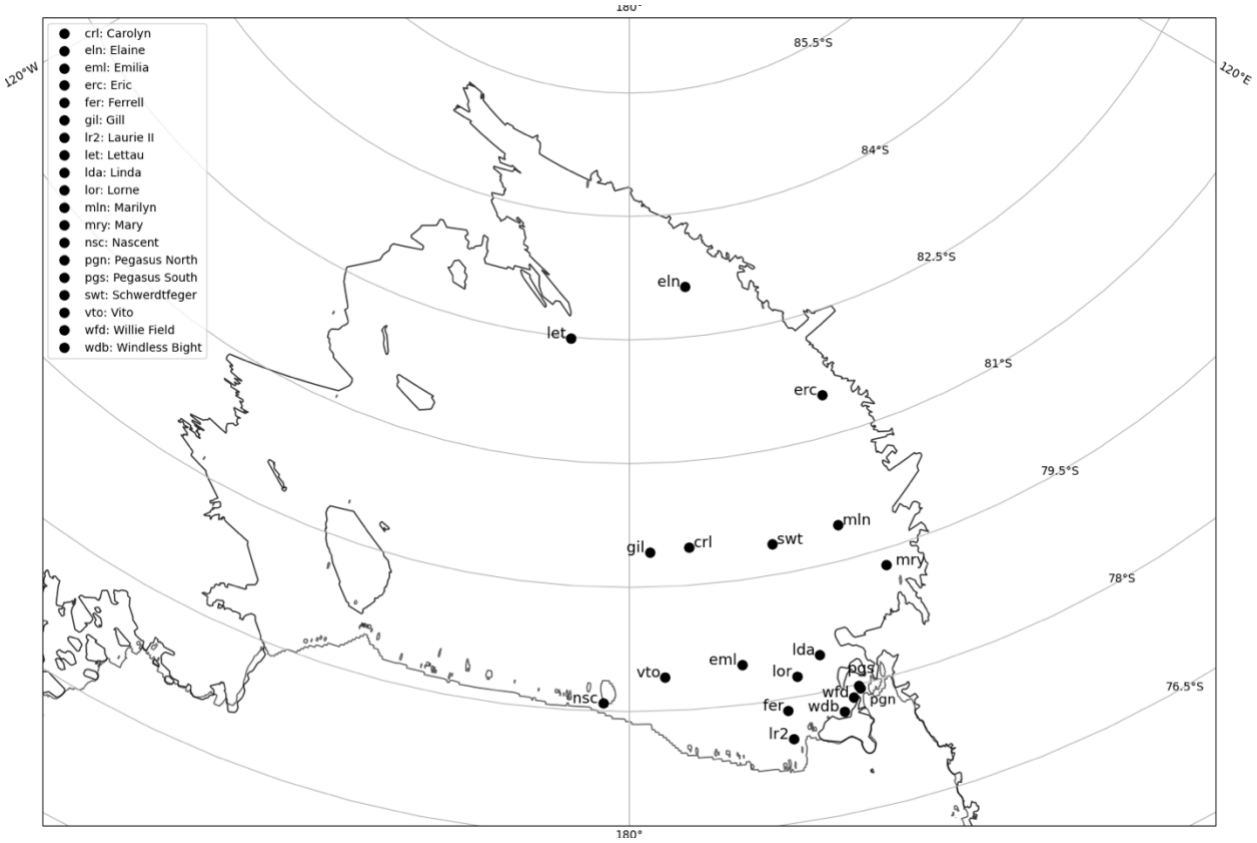

Figure 1.2: All AWS installed on the Ross Ice Shelf in 2007.

One noted feature of the Antarctic climate, at odds with the rapid warming observed in the RWEW for this study, is the coreless winter, where monthly mean temperatures drop sharply in

the autumn followed by relatively uniform, cold temperatures until spring (van Loon 1967, Thompson 1969, Schwerdtfeger 1970, Wendler and Kodama 1993, Lazzara et al. 2012b). Wendler and Kodama (1993) studied the coreless winter by comparing AWS observations in Adelie Land along a sloped surface, ranging from the coast inland to Dome C in East Antarctica. They note that, in winter, there is a slight increase in the annual mean temperature cycle at D-10 AWS, near the coast. They denote this as a bump in the second harmonic of the annual temperature, a feature noted similarly at the South Pole in Lazzara et al. (2012b). This slight increase in wintertime temperature has also led to the characterization of a "first-" and "second-winter", during which the Antarctic temperature trends at certain sites can be split into two regimes, the former being slightly warmer than the latter (Lazzara et al. 2012b; Costanza et al. 2016).

Antarctica is also known for a strong and persistent wind regime, typically referred to as katabatic winds (Parish and Cassano 2003). Ball (1956) used observations near Commonwealth Bay, Antarctica (near Adelie Land) to model and study katabatic winds, noting that katabatic winds are formed by a cold, thin layer of air that is cooled by radiation at the surface and then flows down the slope. Parish and Cassano (2003) used the fifth-generation Pennsylvania State University-National Center for Atmospheric Research Mesoscale Model (MM5) to study how katabatic winds are formed and sustained over Antarctica. In a simulation initialized with zero pressure gradient force (PGF), longwave radiative flux divergence acts to cool the surface and overlying lowest layers of the atmosphere, producing a negatively buoyant layer of air adjacent to the ice surface. This results in the establishment of a PGF near the surface that is responsible for the downslope acceleration of the wind. Katabatic winds are not ubiquitous, however, and can break down for various reasons including solar heating, the lack of a sloped surface, and a breakdown of the surface inversion due to the passage of synoptic-scale disturbances.

Just as wind regimes vary throughout the Antarctic, temperature regimes vary depending on various factors as well. Costanza et al. (2016) conducted a climatology of UW-Madison AWS on the RIS, analyzing temperature, pressure, and wind speed and direction observations. They separated the RIS into three representative regions: central, coastal, and along the Transantarctic Mountains. AWS in the central RIS were found to observe the coldest mean temperatures and the lowest mean resultant (vectorial average) wind speeds. The warmest mean temperatures and highest mean resultant wind speeds were observed at AWS along the Transantarctic Mountains, and the lowest mean pressures were observed at AWS in the coastal region.

On the East Antarctic Plateau, where the katabatic wind regime dominates in the winter, deviations from the coreless winter temperature pattern can occur because of large and rapid temperature increases. These temperature increases have been noted throughout the continent, and the causes range from the passage of certain synoptic-scale features to the interaction of such passages with the severe topography of the continent. Hirasawa et al. (2000, 2013) studied a rapid increase in surface air temperature observed at Dome Fuji Station (the Japanese Antarctic Research Expedition staffed station), Enderby Land, in June 1997. They note that, at the onset of the warming, there was a stationary 500-hPa high-pressure center situated over Dome Fuji. This blocking ridge was formed at the leading edge of a quasi-stationary Rossby wave train that propagated from lower latitudes and along the Southern Ocean. Strong, poleward geostrophic winds developed at the leading edge of this blocking high and led to transport of clouds and warm, moist air from the lower latitudes into the Dome Fuji region. As a result, the temperature at Dome Fuji Station increased from approximately -70° C to approximately -30° C in two days. As mentioned previously, in Adelie Land, Wendler et al. (1993) studied AWS temperature observations from five AWS in austral winter. These AWS are aligned along the ice sheet slope in

Adelie Land from the Adelie Coast inland to Dome C (elevation 3250 m). The authors found that rapid temperature increases were accompanied by high winds for AWS on flat ground, i.e. Dome C. For AWS on a sloped surface, they found the wind direction shifted from a downslope, katabatic regime during cold spells to cross-slope during warm spells.

As indicated previously, there are features of the large-scale Antarctic atmospheric circulation that can affect smaller-scale atmospheric features over the continent. On the East Antarctic Plateau, studies have found that the main cause for rapid surface warming is a synoptic-scale blocking high at upper-levels, leading to poleward flow of warm air (Hirasawa et al. 2000, 2013). In the West Antarctic and RIS regions, the Amundsen-Bellingshausen Seas Low (ABSL) is a climatological low-pressure feature in the Amundsen-Bellingshausen Seas region that supports the poleward flow of air (Hosking et al. 2013). They note that the ABSL shifts westward towards the Ross Sea from summer to winter. This shifts the area of poleward, meridional flow from the Ellsworth Land/Antarctic Peninsula region to the Marie Byrd Land/Siple Coast region.

For the RIS, the synoptic-scale setup leading to rapid warming typically results from the passage of cyclonic disturbances in the Ross Sea (Coggins et al. 2014). These cyclonic disturbances may originate from a prominent region of cyclogenesis upstream of the RIS off the coast of Adelie Land (Bromwich et al. 2011). The authors in this study investigated how cyclones form off the coast of Adelie Land using output from the Antarctic Mesoscale Prediction System (AMPS) for the years 2003-2005, finding two primary patterns: secondary development and lee cyclogenesis. The former is dependent on enhanced low-level cyclonic vorticity and baroclinicity resulting from an existing synoptic-scale cyclone to the west of Adelie Land, coastal barrier winds, and katabatic winds. The latter occurs on the cyclonic-shear side of the Adelie Land katabatic jet, where a low-level warm potential temperature anomaly sets up a lee trough that propagates

eastward off Cape Adare and into the Ross Sea with the arrival of upper-level synoptic-scale forcing.

These synoptic-scale disturbances have complex effects on the atmospheric patterns in the RIS region, mostly owing to the complex topography of the region. Coggins et al. (2014) produced a synoptic climatology of the RIS and Ross Sea using ERA-Interim (ERA-I) reanalysis output of 10-m wind, 2-m temperature, and mean sea level pressure, for the years 1979 through 2011. They used a k-means clustering algorithm to show maps of atmospheric conditions that reflect patterns repeated in the data, finding that one prevalent feature in the wind field is a strong low-level jet propagating from the southern tip of the RIS and Siple Coast and northward along the Transantarctic Mountains. This resembles the Ross Ice Shelf air stream (RAS), a prominent feature of the low-level wind field over the RIS (Parish et al. 2006, Seefeldt and Cassano 2008). These studies have found that the RAS begins at the southern tip of the RIS due to a confluence of drainage flow from the East and West Antarctic plateaus. Synoptic-scale disturbances can enhance the pressure gradient over the RIS along the Transantarctic Mountains, thereby strengthening the RAS. Seefeldt and Cassano (2012) found that there is strong seasonality to the RAS, with it being more common in the winter. Additionally, its strength is dependent on the position of the cyclone in the Ross Sea. By examining the meteorological environment before, during, and after the RWEW in this study, the climatological temperature, wind, and cyclone patterns in and around the RIS can be used to understand the mechanisms by which such a rapid and large-scale surface temperature warming occurred.

For the event in this study, AWS observational data (temperature, pressure, wind speed and direction) from the 14 AWS that observed a warming event are studied. Figure 1.3 shows temperature observations at Schwerdtfeger, which observed a warming event from 02:30 UTC 13

July to 13:50 UTC 15 July. The preceding synoptic environment consisted of a stationary surface cyclone in the Ross Sea, a ridge upstream in the Amundsen Sea, and a strong zonally oriented baroclinic zone. A cyclone propagating off Cape Adare merged with the existing surface cyclone, reorienting the baroclinic zone to advect warm air towards the RIS. The wind field of the RIS was modified due to the approaching cyclone, enhancing the effects of warming along the Transantarctic Mountains. The European Centre for Medium Range Weather Forecasts (ECMWF) Reanalysis Interim (ERA-I; Dee et al. 2011) and version 5 (ERA5; Hersback et al. 2020) data are used to assess the upper- and lower-level synoptic setup to this event to investigate how this warming event compared to others in the RIS and the Antarctic. Chapter 2 describes the data and methodology used for this study, including a discussion of the AWS, reanalysis, and satellite data. Chapter 3 consists of a case study analysis of the 12-15 July 2007 RWEW over the RIS. Chapter 4 consists of a discussion of this case study RWEW, how it relates to previously documented warming events in the Antarctic, and the roles of turbulent mixing, warm air advection, and cloud cover contributing to this RWEW. Chapter 5 outlines future work, including investigation of the large-scale influences on this warming event and how that can be used to understand previous and future warming events in the Antarctic.

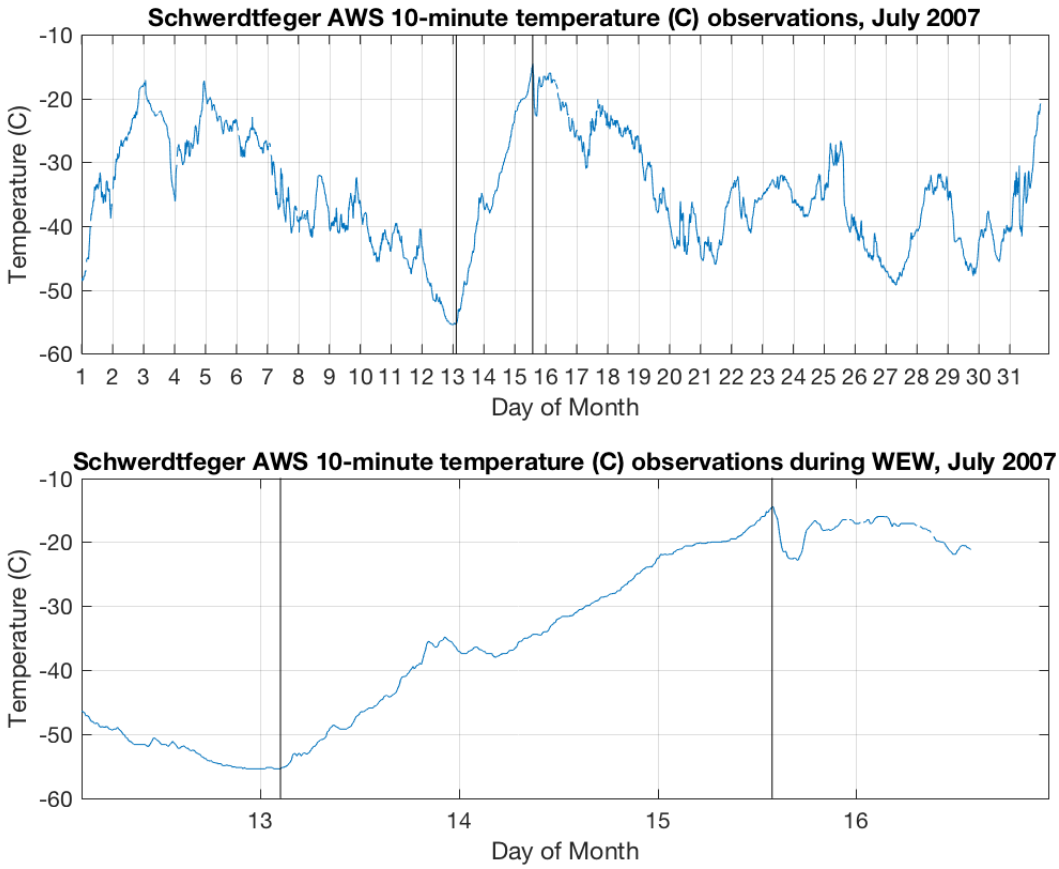

Figure 1.3: Temperature observations at Schwerdtfeger for July 2007 (top) and 12-16 July 2007 (bottom). The black vertical lines denote the beginning and ending of the warming event.

CHAPTER 2: DATA AND METHODOLOGY

Observational data from the UW-Madison AWS network were examined to determine whether a warming event occurred in the study period of 12-15 July 2007. These data are 10-minute, quality-controlled observations (q10) that include temperature, pressure, wind speed, and wind direction. The beginning and ending of the warming events were subjectively determined. When there was a temperature increase of 30° C or greater in five or fewer days, the beginning of that temperature increase was chosen based on when the trend switched from neutral or negative to positive. The ending of the event was chosen when the trend switched from positive to neutral or negative. There were 22 AWSs installed on the RIS or in the Ross Island region during the time of this RWEW. It was determined that 14 distinct AWSs observed this warming event. If an AWS was missing observational data during the study period of interest and hence did not have a continuous enough data set, it not included in this study. Each of the 14 AWS observing warming had quality-controlled data available that were nearly uninterrupted throughout the event. Table 1 lists each AWS that observed the warming, its start and end times, and the observational data at the beginning and end of the warming. For computing climatological statistics for the 14 AWSs, all available 3-hourly quality-controlled data in the period 1991-2020 were used. The 3-hourly time resolution was chosen because there is a more complete record of quality-controlled data at this increment than at the 10-minute resolution. For comparing AWS data to ERA5 reanalysis data (as we will do in subsequent portions of the analysis), 1-hourly quality-controlled AWS data were used to match ERA5's time resolution.

For the synoptic meteorological analysis of the RWEW, ERA-I and ERA5 reanalysis output, CloudSat and CALIPSO satellite retrievals, and infrared satellite composite imagery were

used. The ERA-I reanalysis data are based on a gridded dataset of recorded climate observations at 0.7° x 0.7° spatial resolution and 6-hourly temporal resolution (Dee et al. 2011). ERA5 reanalysis data are at 0.25° x 0.25° spatial resolution (31 km), 1-hourly temporal resolution, and are based on the Integrated Forecasting System Cy41r2 and observational data assimilation to model the atmosphere (Hersback et al. 2020). The ERA5 reanalysis is one of the better-performing reanalyses over Antarctica. Gossart et al. (2019) evaluated near-surface variable output from four reanalyses: ERA5, ERA-Interim, the Climate Forecast System Reanalysis (CFSR), and the Modern-Era Retrospective Analysis for Research and Applications, version 2 (MERRA-2). ERA5 was shown to best capture the seasonal cycle of near-surface temperature, with the smallest bias relative to observations. Zhu et al. (2021) did an assessment of ERA5 and ERA-I surface air temperatures by comparing the two reanalyses' output to observations, including numerous AWS used in this RWEW study. The authors found ERA5 surface air temperature data correlated well with observations, including capturing long-term surface air temperature trends. Tetzner et al. (2019) compared ERA5 and ERA-I reanalysis output to AWS data in the southern Antarctic Peninsula and Ellsworth Land regions and found similar results in ERA5 surface air temperature performance. The authors also found ERA5 accurately captured the surface wind regime above 1000 m, but coastal regions exhibited a wind bias of -1.48 m s^{-1}. Since the Ross Sea borders the RIS, and RIS surface elevations are near sea level, it can be considered a coastal region, and these ERA5 wind biases will be considered when using ERA5 10-m wind data.

To further test the validity of ERA5 reanalysis data for this study, correlations between AWS observations and ERA5 data were calculated. A nearest-neighbor approach was employed between hourly AWS observations and ERA5 data for temperature, pressure, and wind speed. The period examined was from 00 UTC 10 July through 23 UTC 17 July to capture the state of the

atmosphere before, during, and after the RWEW (Fig. 2.1). Temperature differences between the AWS observations and ERA5 were generally within +/-4° C though sometimes reached +/-8° C. ERA5 mean sea level pressure values were greater than AWS pressure observations at each site, typically by approximately 5-10 hPa. During each distinct warming event, correlations were calculated between hourly AWS observations and hourly ERA5 data for temperature, pressure, and wind speed (Fig. 2.2). Strong correlations were found for temperature (most with an r^2 value greater than or equal to 0.92) and pressure (not shown; most with an r^2 value greater than or equal to 0.99). For wind speed (not shown), weaker correlations were found between AWS wind speed observations and ERA5 10-m wind speed, with about half of the r^2 values between 0.40 and 0.80. Given these correlation results and considering previous work on the validity of ERA5 2-m temperatures, the ERA5 2-m temperatures were considered to accurately represent the magnitude and trends of temperature. The ERA5 mean sea level pressure accurately represents the pressure trends though they exhibit a positive bias. Since the wind speeds were at two different levels (approximately 2-m for AWS observations, 10-m for ERA5) and the correlations were satisfactory, the ERA5 10-m winds were deemed to fairly represent the near-surface wind field during the RWEW.

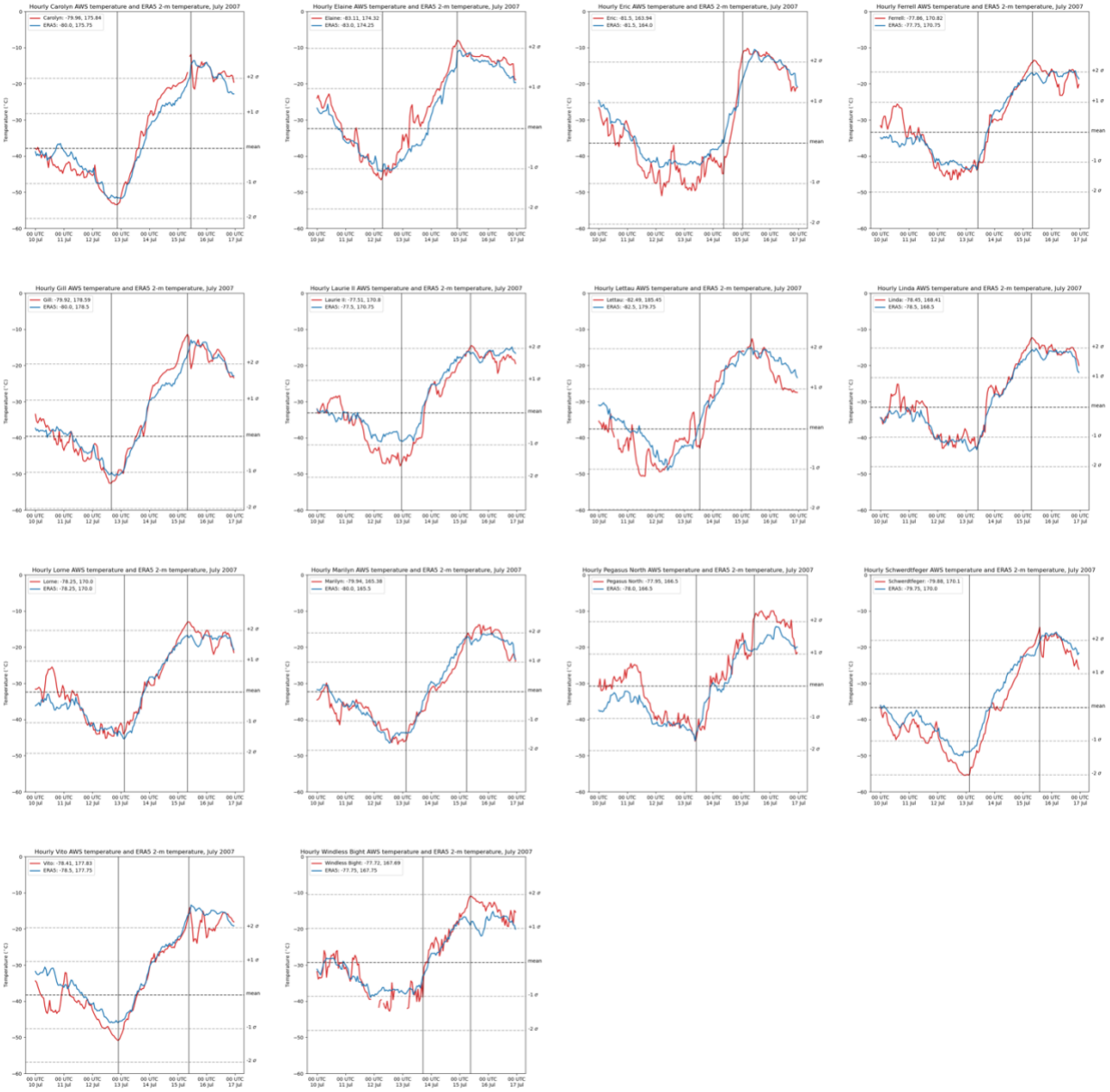

Figure 2.1: Hourly temperatures of AWS observations (red) and ERA5 2-m temperatures (blue) (° C) from 10 through 17 July 2007, with separate plots for each of the 14 AWS observing warming. Black vertical lines denote the beginning and ending of the warming events. Horizontal dashed lines indicate the respective AWS climatological July monthly mean temperature and +/-1 and +/-2 standard deviations from the mean. The legend includes the AWS coordinates and the ERA5 coordinates of the nearest grid cell.

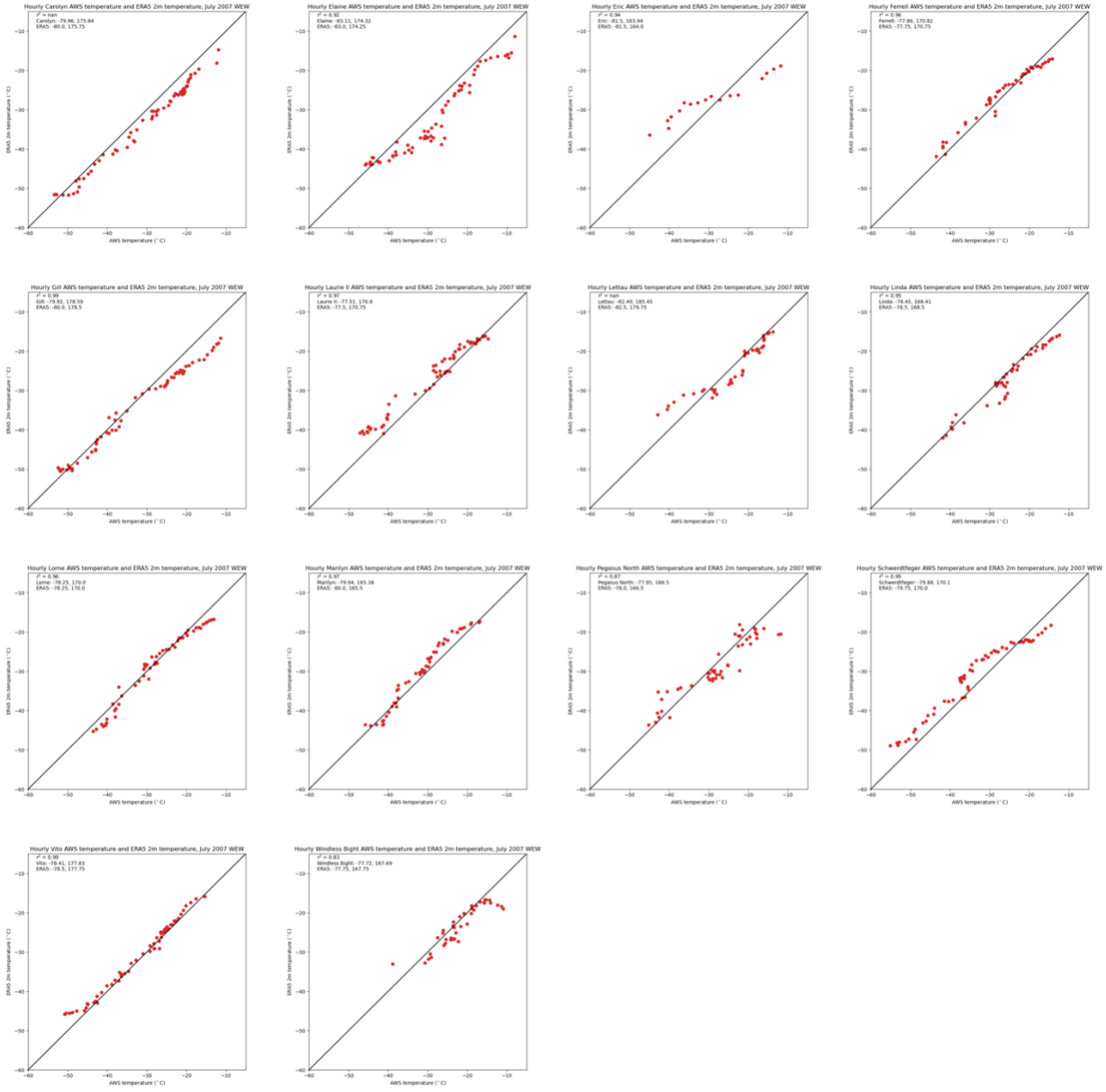

Figure 2.2: Correlations between hourly AWS temperature observations and ERA5 2-m temperatures during each respective warming event. The black diagonal line denotes a 1:1 correlation. The legend includes the AWS coordinates and the ERA5 coordinates of the nearest grid cell.

The following ERA-I reanalysis output data were used to study the synoptic-scale evolution of this RWEW: 300-hPa geopotential height and wind; 500-hPa geopotential height, temperature, wind, and relative vorticity; 850-hPa geopotential height, temperature, wind, specific

humidity, and relative vorticity; and mean sea level pressure, 10-m winds, and 2-m temperature. ERA5 2-m temperatures and 10-m winds were used. Infrared satellite composite imagery over the Antarctic region from the Antarctic Meteorological Research Center (AMRC) (Kohrs et al. 2014; Lazzara et al. 1999) were used to determine locations of surface low pressure systems and cloud signatures. During the study period, the temporal resolution for this imagery is 3-hourly; the spatial resolution is 5 km nominal resolution at 60° South.

Satellite data retrievals from CloudSat and Cloud-Aerosol Lidar and Infrared Pathfinder (CALIPSO) (L'Ecuyer and Jiang 2010), part of the National Aeronautics and Space Administration (NASA) Afternoon-Train (A-Train) group of polar-orbiting satellites, were used to assess the cloud characteristics and radiative flux properties above the RIS and surrounding region for this RWEW. CloudSat uses its 94-GHz Cloud Profiling Radar (CPR) to provide information about cloud structure. Reflectivity (dBZ) from the 2B-GEOPROF R05 product (Marchand et al. 2008) were used. CALIPSO's Cloud Aerosol Lidar with Orthogonal Polarization (CALIOP) (532- and 1,064-nm wavelengths) is sensitive to the distribution of aerosols and thin clouds. Combining data from the CPR and lidar allows for the reliable determination of cloud phase and estimation of cloud radiative influence. Output examined were cloud phase (liquid, mixed, or iced) from the 2B-CLDCLASS-lidar R05 product (Wang et al. 2012) and downwelling longwave (W m^{-2}), and bottom of the atmosphere longwave cloud radiative effect (W m^{-2}) from the 2B-FLXHR-LIDAR (Henderson et al. 2013). ECMWF temperature and land surface type were plotted to supplement analysis of the satellite observations along the satellite pass. The ECMWF temperatures are a product from the ECMWF-AUX dataset, which is an intermediate product for the CloudSat Data Processing Center (DPC) that contains the set of ancillary ECMWF state variable data interpolated to each CloudSat cloud profiling radar bin and the input data is obtained

from the AN-ECMWF dataset provided by the ECMWF (CloudSat DPC, 2022). The time stamps for CloudSat/CALIPSO plots used in this study are from the midpoint of the respective swath path.

CHAPTER 3: CASE STUDY ANALYSIS

3.1 AWS observations

From 6:20 UTC 12 July 2007 through 14:40 UTC 15 July 2007, 14 AWS on the RIS observed warming events. Figure 3.1a shows the location of each AWS and timing of warming event onset, with the colors corresponding to when the warming began for each AWS. Figure 3.1b shows the topographical elevation of Antarctica and the names of geographical features referenced throughout the remainder of this paper. The first AWS to observe a warming event was Elaine (eln), on the southern end of the RIS near the Transantarctic Mountains, starting at 6:20 UTC 12 July (Table 1). Throughout 12 July, AWS further north on the RIS began observing warming (Gill (gil), Carolyn (crl), Vito (vto), Laurie II (lr2)). Early on 13 July, the several AWSs near Ross Island, at the northwest corner of the RIS, began observing warming (Schwerdtfeger (swt), Lorne (lor), Marilyn (mln), Ferrell (fer), Pegasus North (pgn), Linda (lda), Windless Bight (wdb)). Midday on 13 July, Lettau (let) began observing warming. The last AWS to begin observing warming was Eric (erc), near the Transantarctic Mountains, starting at 8:50 UTC 14 July. The warming events for all AWS ended on 15 July, except for Elaine, which ended on 14 July. Figure 3.2 shows AWS observation plots of temperature, pressure, wind speed, and wind direction, for the duration of the warming event. For each AWS, as the temperature increased throughout the event, the pressure decreased. For wind speeds at most AWSs, as the warming event progressed, the wind speeds increased through the middle of the event and then plateaued; for others, the speed did not change much throughout. Wind directions throughout the warming events were steady, particularly for AWS with high wind speeds. Table 2 shows the temperature correlations to pressure and wind speed at each AWS during the warming event. There were negative correlations

between temperature and pressure for all AWS, and all except Elaine showed a strong negative correlation of greater than -0.90. This suggests a strong relation to the arrival of a low pressure system coincident with warming. The correlations to wind speed were more varied, however. This could be due to several factors, including varying influence from the larger-scale synoptic environment, varying topographical influences, and instrumentation malfunction.

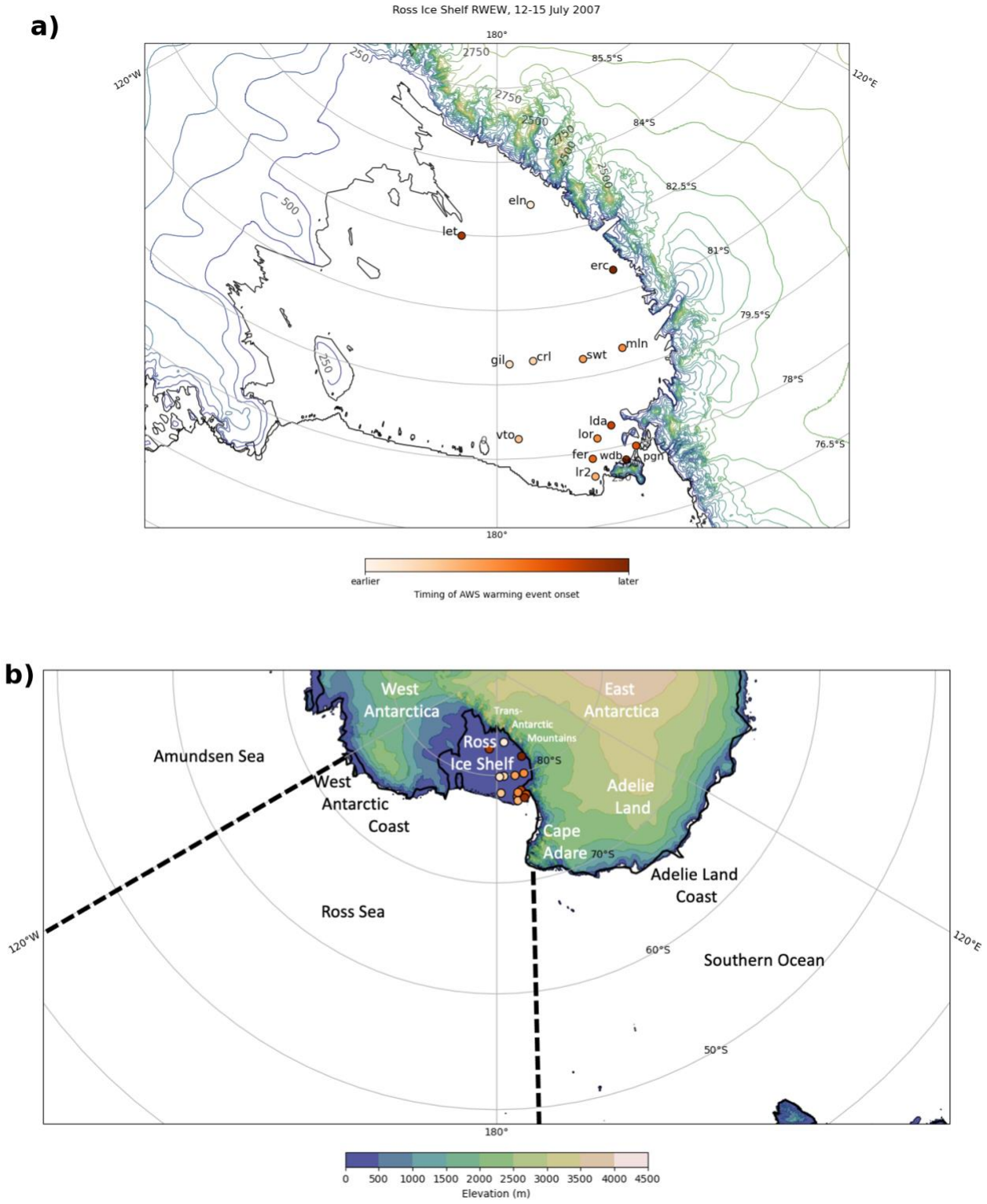

Figure 3.1: a) Map of the RIS with each AWS location color-coded based on onset of warming event, and topographical contours every 250 m and color-coded as shown in the legend in b), and b) as in Fig. 1b, but with the AWS locations included, color-coded as in a).

Table 1: Locations and observational data for each AWS observing a warming event in the RWEW, listed in alphabetical order.

AWS	ID	Latitude	Longitude	Time, start (UTC)	Time, end (UTC)	Temp, start (°C)	Temp, end (°C)	Pressure, start (hPa)	Pressure, end (hPa)
Carolyn	crl	-79.964	175.842	20:20 12 Jul	11:00 15 Jul	-53.6	-11.9	990.0	974.3
Elaine	eln	-83.111	174.316	6:10 12 Jul	22:10 14 Jul	-47.2	-7.9	999.1	978.2
Eric	erc	-81.504	163.939	8:40 14 Jul	1:30 15 Jul	-45.4	-10.8	NA	977.4
Ferrell	fer	-77.860	170.819	9:20 13 Jul	8:30 15 Jul	-44.5	-13.5	1003.5	973.9
Gill	gil	-79.922	-178.586	15:40 12 Jul	8:20 15 Jul	-52.8	-11.1	999.3	975.9
Laurie II	lr2	-77.509	170.797	22:10 12 Jul	9:40 15 Jul	-48.0	-14.2	1004.3	974.9
Lettau	let	-82.486	-174.553	12:50 13 Jul	8:40 15 Jul	-43.1	-12.4	1003.4	987.5
Linda	lda	-78.453	168.410	9:40 13 Jul	6:50 15 Jul	-42.9	-12.4	1005.1	974.6
Lorne	lor	-78.250	170.000	2:40 13 Jul	8:10 15 Jul	-44.0	-13.0	1004.6	974.0
Marilyn	mln	-79.935	165.378	2:40 13 Jul	6:30 15 Jul	-46.4	-15.6	1002.8	973.6
Pegasus North	pgn	-77.957	166.515	9:20 13 Jul	11:30 15 Jul	-46.0	-10.0	1010.7	980.9
Schwerdtfeger	swt	-79.875	170.105	2:30 13 Jul	13:50 15 Jul	-55.4	-14.5	1000.9	975.8
Vito	vto	-78.501	177.753	21:50 12 Jul	9:30 15 Jul	-51.0	-13.6	1002.7	975.3
Windless Bight	wdb	-77.723	167.692	16:50 13 Jul	9:00 15 Jul	-41.2	-10.9	1002.1	977.0

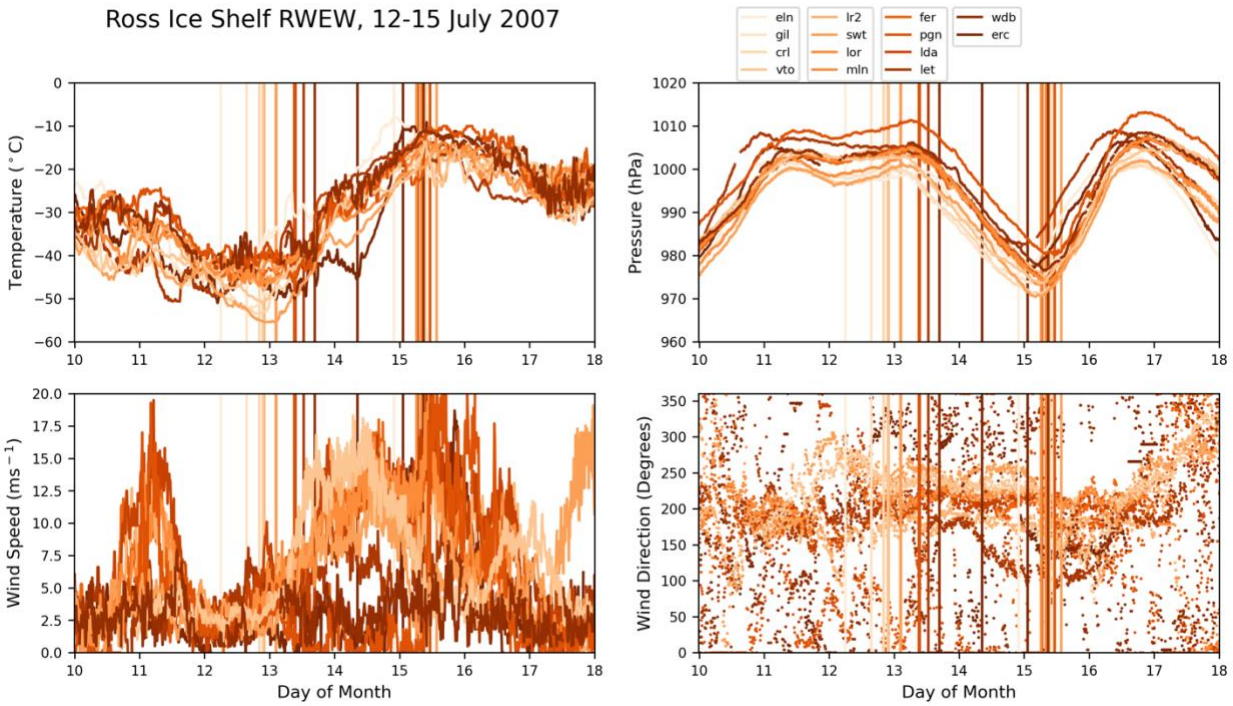

Figure 3.2: AWS observations from 10-17 July 2007 of temperature (° C) (upper left), pressure (hPa) (upper right), wind speed (m s^{-1}) (lower left), and wind direction (degrees) (lower right). All data plotted are color-coded as in Fig. 3.1a.

Table 2: AWS q10 temperature correlations with pressure and wind speed during each warming event.

AWS	Temperature-Pressure	Temperature-Wind Speed
Carolyn	-0.96	NA
Elaine	-0.88	NA
Eric	-0.98	0.79
Ferrell	-0.98	0.55
Gill	-0.98	NA
Laurie II	-0.95	0.6
Lettau	-0.96	-0.06
Linda	-0.93	0.77
Lorne	-0.99	0.83

Marilyn	-0.97	NA
Pegasus North	-0.92	0.43
Schwerdtfeger	-0.97	0.05
Vito	-0.98	0.45
Windless Bight	-0.90	0.25

3.2 Synoptic assessment

Two days prior to the beginning of the RWEW, at 00 UTC 10 July, collocated geopotential height minima at 300, 500, and 850 hPa and a mean sea level pressure minimum were situated in the northeast Ross Sea with strong northerly flow downstream (Fig. 3.3a, b, c, and d). At 300 hPa (Fig. 3.3a), a large geopotential height gradient extended from the Ross Sea height minimum southeastward to the West Antarctic coast where a local wind speed maximum, or jet streak, was located. At lower levels in this same region, a large temperature gradient was established. This was due to warm air advection from the northerly flow, as the wind barbs at 500 and 850 hPa were oriented nearly perpendicularly to isotherms just southeast of the low (Fig. 3.3b and c). Near the surface (Fig. 3.3d), the warm air advection was east and southeast of the Ross Sea low. The isotherms indicate the baroclinic zone at 500 hPa ranged from -28° C on the northern edge to -40° C on the southern edge; at 850 hPa it ranged from 0° C to -20° C; and at the surface it ranged from 0° C to -16° C. The 850-hPa relative vorticity indicates two cyclonic relative vorticity minima within the Ross Sea geopotential height minimum, the southern of which extended along the baroclinic zone. A distinct trough axis in mean sea level pressure was at this same location. At the southern tip of the RIS, there was another collocated upper-level height minimum and surface low. A collocated local 850-hPa minimum in cyclonic vorticity suggests a robust cyclonic circulation. The broad influence of this cyclonic circulation can be seen at 300 and 500 hPa, with the northern

portion of this low providing a barrier upon which the northerly flow in the Ross Sea was deflected southeastward. This limited the southward extent of the baroclinic zone in the Ross Sea. Upstream of the Ross Sea low in the Southern Ocean, slight curvature in the flow was evident in the 300- and 500-hPa geopotential height fields along the Adelie Land coast. A 300-hPa ridge with a jet streak on the ridge axis was just off the coast of Cape Adare. A weak trough at those levels was just upstream of that ridge. At 850 hPa and the surface, no such ridging was evident but a there was a collocated trough and a zonally elongated low, just north of the Adelie Land Coast. A tight baroclinic zone extended from the elongated low eastward towards the southern portion of the Ross Sea cyclone. This baroclinic zone was less evident at 850 hPa and essentially nonexistent at 500 hPa. In the Ross Sea, the infrared satellite composite image (Fig. 3.3e) shows a comma shape of bright white, high-altitude clouds associated with the Ross Sea cyclone. These high clouds also extended southeastward towards the West Antarctic coast in the region of the baroclinic zone. Over the southern Ross Sea and RIS, there were no major cloud signatures, indicating either clear skies or thin, low clouds. Since this is infrared satellite imagery, and there was sea ice, the ice shelf, and continental ice in the region, it can be difficult to distinguish low clouds from the surface as the temperatures of the clouds and surface may be identical. Upstream in the Southern Ocean off the Adelie Land Coast, there was a somewhat organized comma-shaped cloud feature associated with the cyclonic disturbance in this region. Atmospheric conditions at the surface were generally calm over the RIS (Fig. 3.3f) with 10-m wind barbs indicating low to calm wind speeds, particularly over the western RIS where the AWS were located. AWS temperature observations were generally in the low to mid -30°s C except for Elaine and Eric along the Transantarctic Mountains, which were in the mid -20°s C.

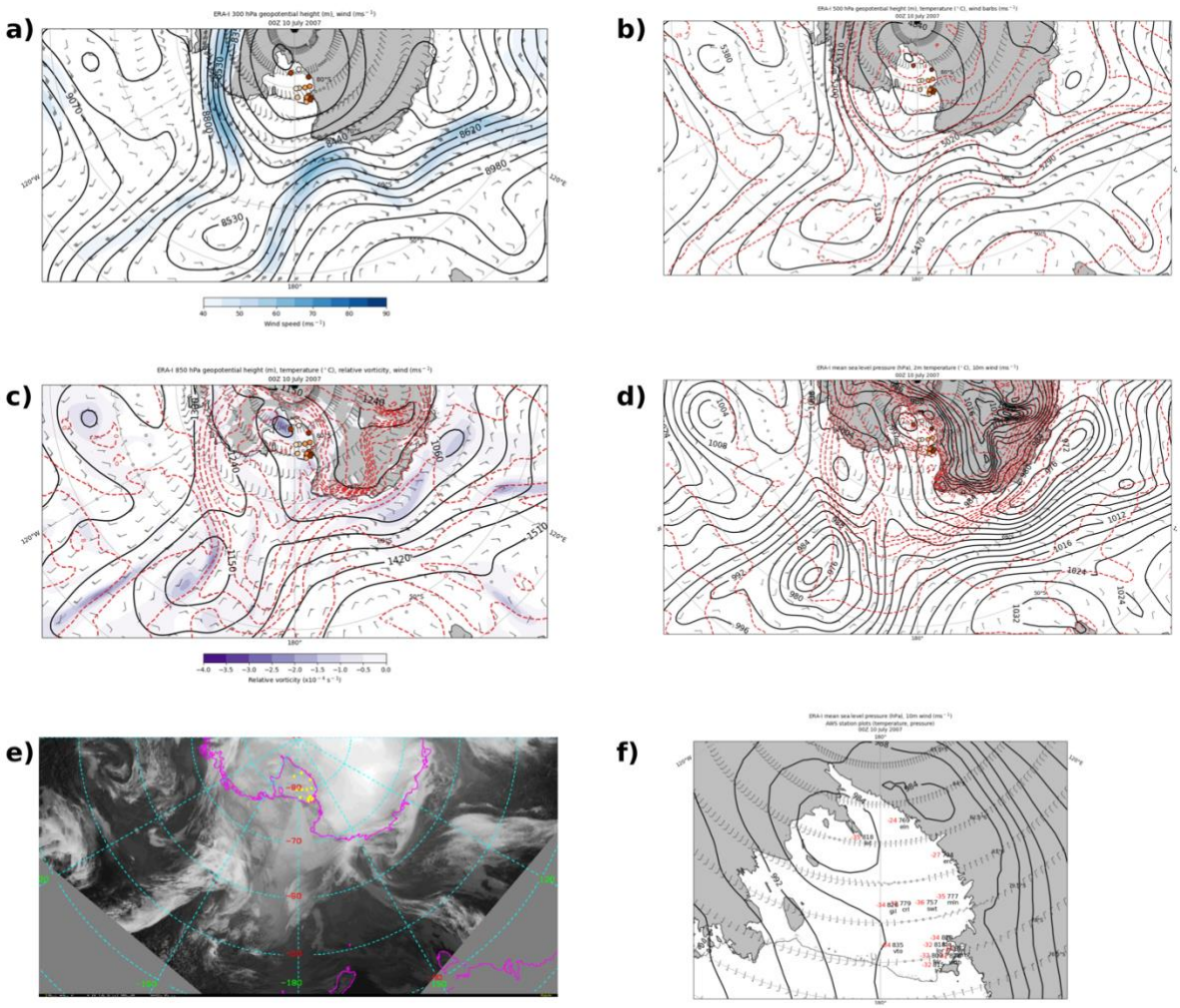

Figure 3.3: ERA-I 00 UTC 10 July a) 300-hPa geopotential height (m) (black contours), wind speed (m s^{-1}) (fill contours every 5 m s^{-1} from 40 to 90 m s^{-1}), wind barbs (m s^{-1}); b) 500-hPa geopotential height (m) (black contours), temperature (° C) (dashed red contours), wind barbs (m s^{-1}); c) 850-hPa geopotential height (m) (black contours), temperature (° C) (dashed red contours), relative vorticity (10^{-4} s^{-1}) (fill contours from -4 to 0 every 0.5), wind barbs (m s^{-1}); d) mean sea level pressure (hPa) (black contours), 2-m temperature (° C) (dashed red contours), 10-m wind barbs (m s^{-1}); e) infrared satellite composite image with yellow dots denoting AWS locations; f) mean sea level pressure (hPa) (black contours), 10-m wind barbs (m s^{-1}), station plots of AWS observations of temperature (° C, red) in upper left and pressure in upper right where the leading two digits are dropped if the pressure is greater than or equal to 1000 hPa and the leading first digit is dropped if the pressure is less than 1000 hPa. For a)-d), geopotential heights are contoured every 90 m, temperatures are contoured every 4° C, and AWS are plotted as in Fig. 3.1a.

At 12 UTC 10 July, in the northern Ross Sea the 300-hPa geopotential height minimum shifted slightly eastward, the 500-hPa minimum stayed in the same approximate location, and the 850-hPa minimum and surface low both shifted slightly southward. A broad ridge downstream in the Amundsen Sea existed at all levels. The 300-hPa jet streak over West Antarctica shifted to a more zonal orientation than at 00 UTC 10 July and was aligned along the West Antarctic Coast. Over the RIS, the collocated height minima and surface low weakened slightly at all levels and shifted poleward. Between the Ross Sea low and the West Antarctic Coast, the baroclinic zones at 500 hPa, 850 hPa, and the surface shifted slightly southward with the 500-hPa baroclinic zone becoming separated from the Ross Sea height minimum. There was still pronounced warm air advection at these three levels, particularly at 850 hPa and the surface as the wind barbs just southeast of the Ross Sea low were oriented nearly perpendicularly to the isotherms. The isotherms at these three levels indicate the baroclinic zone at 500 hPa ranged from -20° C to -36° C; at 850 hPa from 0° C to -16° C; and at the surface from 0° C to -12° C nearest the Ross Sea low and strengthened southeastward along the trough axis and towards the West Antarctic Coast. While the surface low weakened slightly, from sub-972 hPa at 00 UTC 10 July to sub-976 hPa, the trough axis along the baroclinic zone remained distinct. The elongated cyclonic relative vorticity at 850 hPa remained along the baroclinic zone. Upstream of the Ross Sea low in the Southern Ocean, a surface cyclone developed off the Adelie Land Coast and was located just north of Cape Adare, with a central pressure of sub-980 hPa. It was situated over a strong baroclinic zone at the surface, though the 850-hPa baroclinic zone was offset to its south, closer to the coast of Antarctica. While the surface cyclone was well-defined, at 850 hPa the geopotential height minimum was relatively broad in geographic extent, and accordingly there were small values of cyclonic relative vorticity. At 300 and 500 hPa, only troughs were evident in this region. The IR satellite composite imagery

indicate a similar cloud structure in the Ross Sea as the low shifted slightly southward. The surface low north of Cape Adare can be seen with a comma shape like that at 12 hours prior, while a band of high clouds upstream progressed southeast towards the Adelie Land Coast. The cloud signatures in the southern Ross Sea and over the RIS were approximately the same. The lack of significant cloud cover and calm atmospheric conditions over the RIS led to further cooling near the surface. The AWS pressure observations indicate surface pressure increased by approximately 9 hPa, the 10-m wind barbs indicate lower wind speeds across the RIS with northerly flow in the eastern RIS and southerly flow in the western RIS, and AWS temperature observations decreased by approximately -5° C across most of the RIS. The AWS temperatures nearest Ross Island in the northwest RIS, however, increased by approximately 6° C.

One day prior to the RWEW, at 00 UTC 11 July, in the northern Ross Sea the geopotential height minima at 300 hPa (Fig. 3.4a), 500 hPa (Fig. 3.4b), and 850 hPa (Fig. 3.4c) shifted slightly eastward. At the surface (Fig. 3.4d), the surface low split into a dipole, with the southern low weakening to sub-980 hPa. At each level, the ridge remained in the same location downstream over the Amundsen Sea, maintaining the northerly flow east of the Ross Sea low. The 300-hPa jet streak progressed southeastward over West Antarctica and weakened in magnitude. The 500-hPa baroclinic zone maintained its position over the West Antarctic Coast. The warm air advection, however, decreased in magnitude as the geopotential height contours were more parallel to the isotherms. This led to a weakened baroclinic zone as the temperature range remained the same (-20° C to -36° C) but covered a larger area. At 850 hPa, the cyclonic relative vorticity associated with the Ross Sea geopotential height minimum decreased slightly as it split into two distinct minima. The minimum associated with the baroclinic zone had separated and progressed southeast towards the West Antarctic Coast. The baroclinic zone increased in magnitude just off the West

Antarctic Coast where the isotherms were most closely packed, and the temperature range increased from 0° C to -20° C. At the surface, the baroclinic zone progressed southward towards the West Antarctic coast as it maintained its temperature range (0° C to -16° C). The sea level pressure trough axis collocated with the surface baroclinic zone was separated from the Ross Sea cyclone, as the pressure gradient was largest along the baroclinic zone. The surface cyclone upstream in the Southern Ocean progressed eastward into the Ross Sea, just west of the existing Ross Sea cyclone, along the surface baroclinic zone as it weakened slightly to sub-984 hPa. The collocated geopotential height troughs at 300 and 500 hPa became more defined, as did the geopotential height minimum at 850 hPa. The 850 hPa cyclonic relative vorticity, however, remained relatively low. Further upstream, near the Adelie Land Coast, a more organized surface cyclone developed. Collocated with this cyclone was a 300-hPa geopotential height minimum, a 500-hPa geopotential height trough, an 850-hPa geopotential height minimum with strong cyclonic relative vorticity, and a surface cyclone with a central sea level pressure of sub-980 hPa. The IR satellite composite imagery in the region (Fig. 3.4e) indicates the disorganization of the Ross Sea low, as the cloud structures separated into a larger region of cloudiness north of 60° South and a region of cloudiness over the West Antarctic Coast associated with the baroclinic zone. The cyclone in the western Ross Sea, which progressed from the Southern Ocean, maintained its comma-shaped cloud structure. The cyclone upstream off the Adelie Land Coast developed a much more distinctive comma shape as it strengthened. There were still minimal cloud features over the southern Ross Sea and RIS. The 10-m wind speeds over the RIS remained low, though the wind direction shifted to southerly over most of the RIS (Fig. 3.4f). AWS temperature observations continued to decrease at most locations, with temperatures ranging from ~-31° C to ~-44° C, with

the colder observations occurring near the center of the RIS. AWS pressure observations continued to increase by approximately 9 hPa, with observations ranging from ~998 hPa to ~1008 hPa.

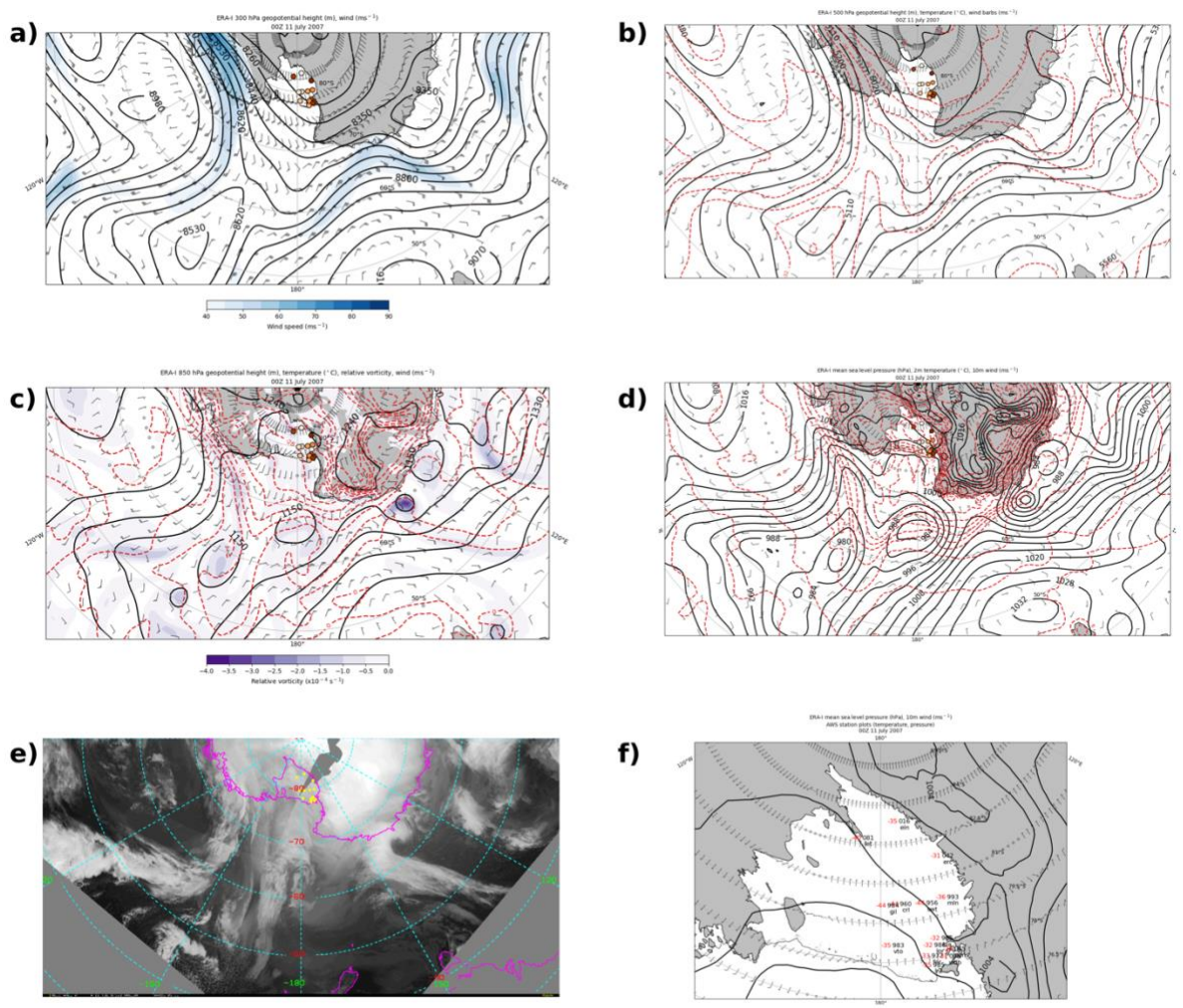

Figure 3.4: As in Fig. 3.3 but for 00 UTC 11 July.

At 12 UTC 11 July, the disturbance that propagated from the Southern Ocean began to merge with the geopotential height minima and the surface low in the Northern Ross Sea (Fig. 3.5a, b, c, and d). The ridge in the Amundsen Sea progressed slightly eastward at 300 hPa (Fig. 3.5a), 500 hPa (Fig. 3.5b), and 850 hPa (Fig. 3.5c). At the surface, the center of the ridge was

located slightly southwestward towards the West Antarctic Coast (Fig. 3.5d) as indicated by the nearly closed-off 1016 hPa isobar contour. The 300-hPa jet streak over the West Antarctic Coast remained in the same location but decreased slightly in magnitude as the geopotential height gradient weakened. Ridge building was evident at this level just southeast of the Ross Sea disturbance as there was increased curvature in the geopotential height contours. At 500 hPa, 850 hPa, and the surface, the warm air advection along the West Antarctic Coast continued at the baroclinic zones. Despite this, the 500-hPa baroclinic zone at this location weakened slightly. At 850 hPa, the warm air advection was strongest along the baroclinic zone near the Amundsen Sea portion of the West Antarctic Coast. With weaker northerly winds along the baroclinic zone between the Ross Sea geopotential height minimum and the West Antarctic Coast, the isotherms were slightly more spread out. At the surface, there were essentially three separate sea level pressure minima in the northern Ross Sea, the deepest of which being at sub-976 hPa on the southeastern portion of the disturbance. The surface baroclinic zone progressed southward towards the West Antarctic Coast but remained stationary in the southern Ross Sea, reaching from the northern Ross Sea disturbance to west Antarctic Coast. Upstream in the Southern Ocean near the Adelie Land Coast, the upper-level support for the cyclone weakened slightly. The 300- and 500-hPa geopotential heights indicated collocated troughs, and the values of 850-hPa cyclonic relative vorticity decreased slightly and became more elongated upstream with the strong baroclinic zone. The surface cyclone maintained its strength at sub-980 hPa as it was collocated with a strong surface baroclinic zone. The IR satellite composite imagery show clouds were still disorganized over the northern Ross Sea (Fig. 3.5e). The cloud band remained over the West Antarctic coast, then stretched northward towards the Ross Sea disturbance, then stretched eastward as the northern-most cloud feature progressed southward. Upstream in the Southern Ocean, off the

Adelie Land Coast the eastern extent of the high-altitude cloud shield associated with the cyclone was just north of Cape Adare. The southern Ross Sea and RIS remained relatively free of any major cloud signatures. The 10-m winds over the RIS remained calm and southerly as a local surface high pressure was centered just north of the northeastern RIS (Fig. 3.5f). AWS pressure observations continued to increase by ~2-3 hPa as AWS temperature observations decreased. The temperatures decreased by ~5-10° C in the central and southern RIS but didn't change much in the northwestern portion.

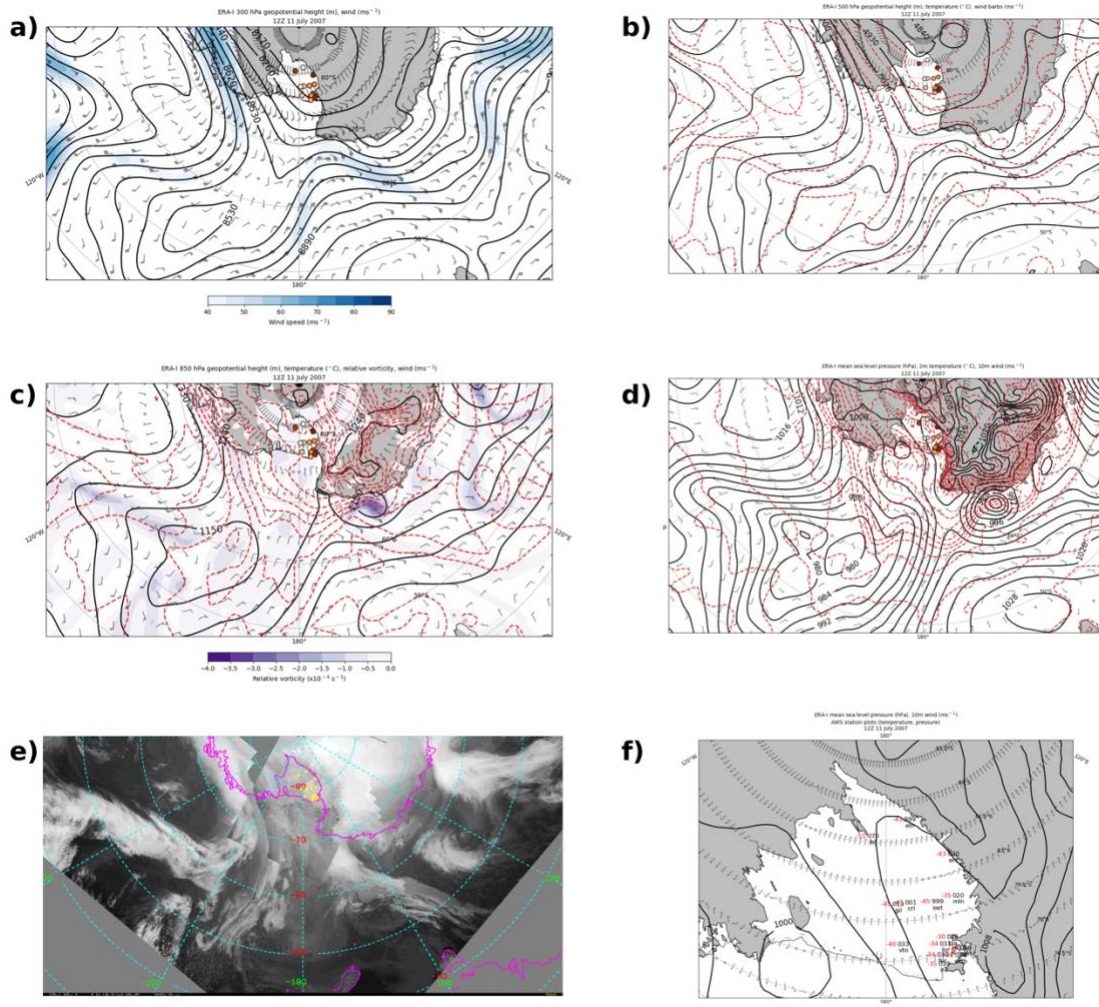

Figure 3.5: As in Fig. 3.3 but for 12 UTC 11 July.

At 00 UTC 12 July, approximately 6 hours before the first warming event began at Elaine, the northern Ross Sea disturbance became more organized. At 300 hPa, the geopotential height minimum deepened to sub-8440 m, the 500-hPa geopotential height minimum deepened to sub-5020 m and became more organized, the 850-hPa geopotential height minimum deepened to sub-1060 m with a local minimum in cyclonic relative vorticity, and the surface disturbance deepened to sub-968 hPa. Collectively, this disturbance moved slightly southward towards the RIS. At all levels, northerly to northeasterly flow remained downstream as the downstream ridge only progressed slightly eastward in the Amundsen Sea. At 300 hPa, the wind maximum over the West Antarctic Coast and West Antarctica continued to decrease in magnitude as the ridge building in the Ross Sea continued south of the disturbance. At 500 hPa, with the ridge progressing slightly eastward in the Amundsen Sea, the warm air advection over West Antarctica decreased as the baroclinic zone progressed over West Antarctica. At 850 hPa, the baroclinic zone just south of the disturbance in the northern Ross Sea, with a temperature range of -4° C to -20° C, slightly increased in magnitude. The geographic extent decreased as the warm air advection continued and the atmosphere cooled in the southern Ross Sea. The surface baroclinic zone remained approximately stationary, reaching from the southern portion of the Ross Sea cyclone southeast to the West Antarctic Coast. Upstream in the Southern Ocean, the cyclonic disturbance progressed eastward, located to the north of Cape Adare. It weakened slightly as the sea level pressure minimum increased to sub-984 hPa and the cyclonic relative vorticity decreased slightly. The 850-hPa and surface baroclinic zones decreased in magnitude but still extended from the cyclone eastward towards the Ross Sea disturbance. The IR satellite composite imagery indicates that the cloud signature associated with the Ross Sea disturbance began to resemble a comma shape, suggesting further development of the cyclone. Clouds remained over the West Antarctic Coast and Ross Sea

region just south of the cyclone, and the cloud shield extending to the east from the Ross Sea cyclone progressed southward. The cloud signature associated with the cyclone upstream off the coast of Cape Adare indicates a large band of high-altitude clouds reached into the Ross Sea region. There were no satellite data at this time over the RIS. The 10-m winds over the RIS indicate light, southerly flow across the majority of the RIS, with calm winds in the northwest portion. The surface pressure was steady as AWS pressure observations did not show much change. AWS temperature observations remained constant or decreased, with some decreasing by ~2-7° C. The coldest observed temperatures were at Lettau and Eric (-48° C).

At 12 UTC 12 July, the geopotential height minima at each level as well as the surface low in the Ross Sea progressed slightly southward towards the RIS. The 300-hPa geopotential height minimum remained at sub-8440 m (Fig. 3.6a), and the ridge building downstream continued, with the ridge extended south of the height minimum. Over the RIS, a local 300-hPa geopotential height minimum remained, with the jet streak likewise remaining approximately stationary over West Antarctica. The southward progression of the 500-hPa geopotential height minimum in the Ross Sea led to warm air advection south of the height minimum that moved the baroclinic zone towards the RIS (Fig. 3.6b). East of Cape Adare in the Ross Sea, the warm air advection also oriented the northern portion of the baroclinic zone meridionally. The 850-hPa geopotential height minimum decreased to sub-970 hPa as it progressed south and strengthened, as indicated by the increased cyclonic relative vorticity (Fig. 3.6c). The baroclinic zone south of the height minimum intensified and progressed slightly southward towards the RIS, with a temperature range of -4° C to -20° C. It was still oriented northwest-to-southeast as it extended to the West Antarctic Coast. The surface cyclone deepened to sub-960 hPa as it shifted westward in the Ross Sea (Fig. 3.6d). This deepening and shift acted to deform the baroclinic zone to its south, tightening and rotating the temperature

gradient near the cyclone clockwise with the increased pressure gradient and increased wind speed. The portion of this baroclinic zone closest to the West Antarctic Coast increased in strength slightly due to the deepening of the cyclone and the 2-m temperatures cooled over the southern Ross Sea, just north of the RIS. The cyclone upstream progressed eastward near the far western Ross Sea. The collocated trough axes at 300 and 500 hPa were just north of Cape Adare. The 850-hPa height minimum began to merge with the Ross Sea disturbance, and the cyclonic relative vorticity decreased slightly. The mean sea level pressure field shows the surface cyclone was still distinct at this time and maintained its strength at sub-984 hPa. Its associated baroclinic zone weakened, however, as the temperature gradient decreased. The IR satellite composite image shows a much more well-defined comma-shaped cloud structure associated with the Ross Sea disturbance (Fig. 3.6e). High clouds extended from the cyclone towards the West Antarctic Coast and began to sweep over the southern Ross Sea. The cloud structure with the upstream cyclone became less organized, as there was no identifiable cyclonic circulation but rather some meridionally-oriented bands of clouds. Over the RIS, the 10-m winds remained southerly and calm, particularly over the western RIS (Fig. 3.6f). While the warming event began at the southern end of the RIS at Elaine, observing -43° C at this time, other AWS further northwest on the RIS continued to cool, with Gill and Schwerdtfeger temperature observing -51° C. Pressure observations generally remained steady across the RIS.

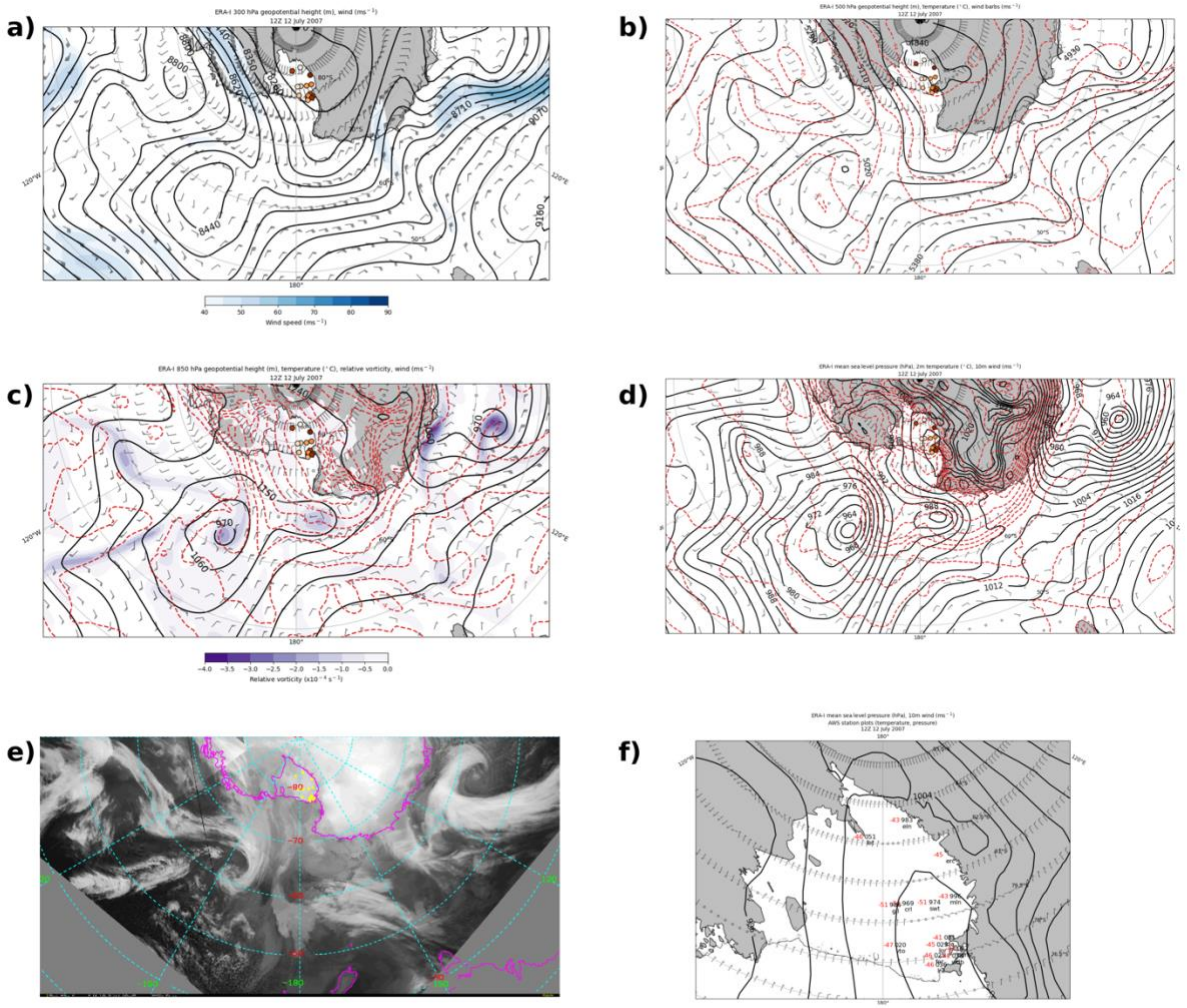

Figure 3.6: As in Fig. 3.3 but for 12 UTC 12 July.

At 00 UTC 13 July, the disturbance in the Ross Sea shifted southward towards the RIS. The 300-hPa geopotential height minimum in the Ross Sea merged with the trough upstream off Cape Adare, as that trough progressed east and increased in spatial extent (Fig. 3.7a). The ridge downstream in the Amundsen Sea moved further south, with the axis extending into West Antarctica. Given this and the geopotential height minimum just west of the RIS, centered over the Transantarctic Mountains in East Antarctica, there was sharp curvature to the flow in the

southern Ross Sea. The jet streak over West Antarctica at the crest of the ridge shifted further poleward. At 500 hPa, the Ross Sea geopotential height minimum also merged with the trough upstream off Cape Adare such that a spatially large geopotential height minimum of sub-4930 m extended from the Ross Sea disturbance southwest towards Cape Adare and poleward over East Antarctica, the Transantarctic Mountains, and the RIS (Fig. 3.7b). This merging of the geopotential height minima, and the southward progression of the ridge in the Amundsen Sea, led to continued warm air advection over the southern Ross Sea that also reached the northern RIS. The baroclinic zone continued rotating clockwise and progressed slightly southward and spanned from the southern Ross Sea to the northeastern RIS. At 850 hPa, the geopotential height minimum in the Ross Sea became elongated southward (Fig. 3.7c). The upstream minimum that originated in the Southern Ocean continued merging in the Ross Sea as its local cyclonic relative vorticity decreased in magnitude. The cyclonic relative vorticity in the Ross Sea disturbance also decreased slightly as a region of cyclonic relative vorticity stretched southward along the developing trough axis and collocated baroclinic zone. The baroclinic zone rotated clockwise, and while the warmer side to the northeast cooled slightly, the cold pool over the RIS expanded such that the baroclinic zone temperature ranged from -8° C to -28° C. At the surface, the Ross Sea cyclone deepened to sub-956 hPa as a trough extended southward to the West Antarctic Coast and the upstream cyclone merged (Fig. 3.7d). Warm air advection southeast of the cyclone rotated the surface baroclinic zone clockwise and increased the temperature gradient, especially in the southern Ross Sea just northeast of the RIS, with temperatures ranging from -8° C to -28° C. The cold pool over the RIS did not shift much in positioning, which also contributed to the strengthened baroclinic zone. The IR satellite composite imagery indicates the center of the Ross Sea cyclone progressed southward, with the cloud shield extending further southeastward over the northeastern RIS (Fig. 3.7e). There

was not much indication of the cyclone upstream as it had merged with the Ross Sea cyclone. The increased pressure gradient approached the northeastern RIS as winds began to increase across the RIS (Fig. 3.7f). The temperature observations at Elaine continued to increase to -34° C while Gill, Carolyn, Vito, and Laurie II began their warming events between 12 UTC 12 July and 00 UTC 13 July, with the warming onset occurring from east to west on the RIS. Most AWS pressure observations increased slightly, particularly in the western and northwestern RIS.

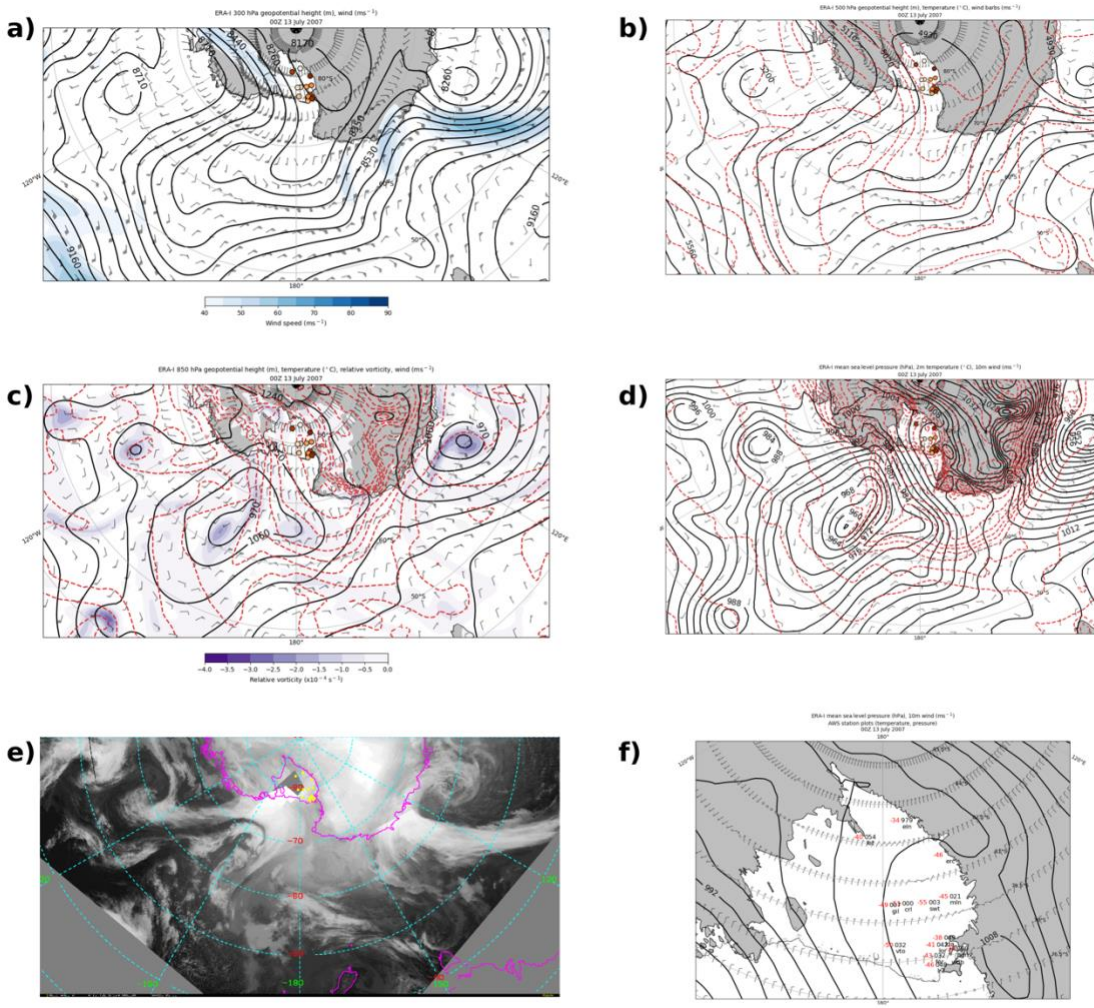

Figure 3.7: As in Fig. 3.3 but for 00 UTC 13 July.

At 12 UTC 13 July, a cyclonic circulation encompassed essentially the entire Ross Sea at all levels as the geopotential height minima and surface cyclone continued strengthening. The 300-hPa geopotential height minimum now had a closed-off circulation and was at 8170 m. The ridge downstream progressed further southward over most of West Antarctica and the RIS. The 500-hPa geopotential height minimum in the Ross Sea deepened to 4840 m. The ridge downstream at that level also progressed southward over West Antarctica and the RIS, with warm air advection over the southern Ross Sea and northern RIS rotating the baroclinic zone further clockwise into a meridional orientation. The 850-hPa geopotential height minimum progressed slightly southward and expanded. The band of cyclonic relative vorticity south of the height minimum increased in magnitude as it extended along the trough axis and baroclinic zone. The baroclinic zone now spanned a temperature range of -12° C to -24° C, a slightly smaller temperature range than 12 hours prior. The spatial extent, however, decreased as it progressed southeast and began to move over the eastern RIS. Temperatures over the western RIS began to increase. The surface cyclone weakened slightly as it progressed southward. The temperature gradient increased, and the trough axis progressed south towards the RIS. Temperatures within the baroclinic zone, in the southern Ross Sea, ranged from -4° C to -24° C. The IR satellite composite image shows the cyclone had a less organized cloud structure, though clouds still extended to the northeastern RIS. With the strengthened and approaching cyclone, the mean sea level pressure gradient increased over the RIS, the 10-m wind speeds increased, especially over the eastern RIS, and AWS pressure observations decreased. AWS temperature observations increased at most AWS as the warming events began at Schwerdtfeger, Lorne, Marilyn, Ferrell, Pegasus North, and Linda. Temperatures ranged from -29° C at Elaine to -42° C at Ferrell. The temperature at Eric remained steady at -46° C.

At 00 UTC 14 July, the 300-hPa geopotential height minimum progressed slightly eastward in the Ross Sea as a ridge upstream with a jet streak in the Southern Ocean developed and expanded into the western Ross Sea (Fig. 3.8a). The ridge downstream remained in the same approximate location. The 500-hPa geopotential height minimum in the Ross Sea deepened to sub-4750 m (Fig. 3.8b). The ridge downstream continued to build over West Antarctica, with warm air advection over the RIS shifting the baroclinic zone further westward across the RIS (Fig. 3.8b). The 850-hPa geopotential height minimum was stationary and maintained its strength as the trough axis and baroclinic zone progressed westward over the RIS (Fig. 3.8c). Although the cyclonic relative vorticity within the trough axis decreased in magnitude, the temperature range remained at -12° C to -24° C. At the surface, the center of the cyclone moved southward and became more circular, maintaining its strength at sub-960 hPa (Fig. 3.8d). The trough axis and baroclinic zone extending south of the cyclone progressed slightly westward over the southern Ross Sea. The IR satellite composite image was missing data in portions of this region, but the cyclone appears to have regained some more organized cloud structure (Fig. 3.8e). Throughout the RIS, AWS pressure observations decreased as the mean sea level pressure gradient increased (Fig. 3.8f). The 10-m winds were southerly over most of the RIS. AWS temperature observations increased as warming events began at Lettau and Windless Bight.

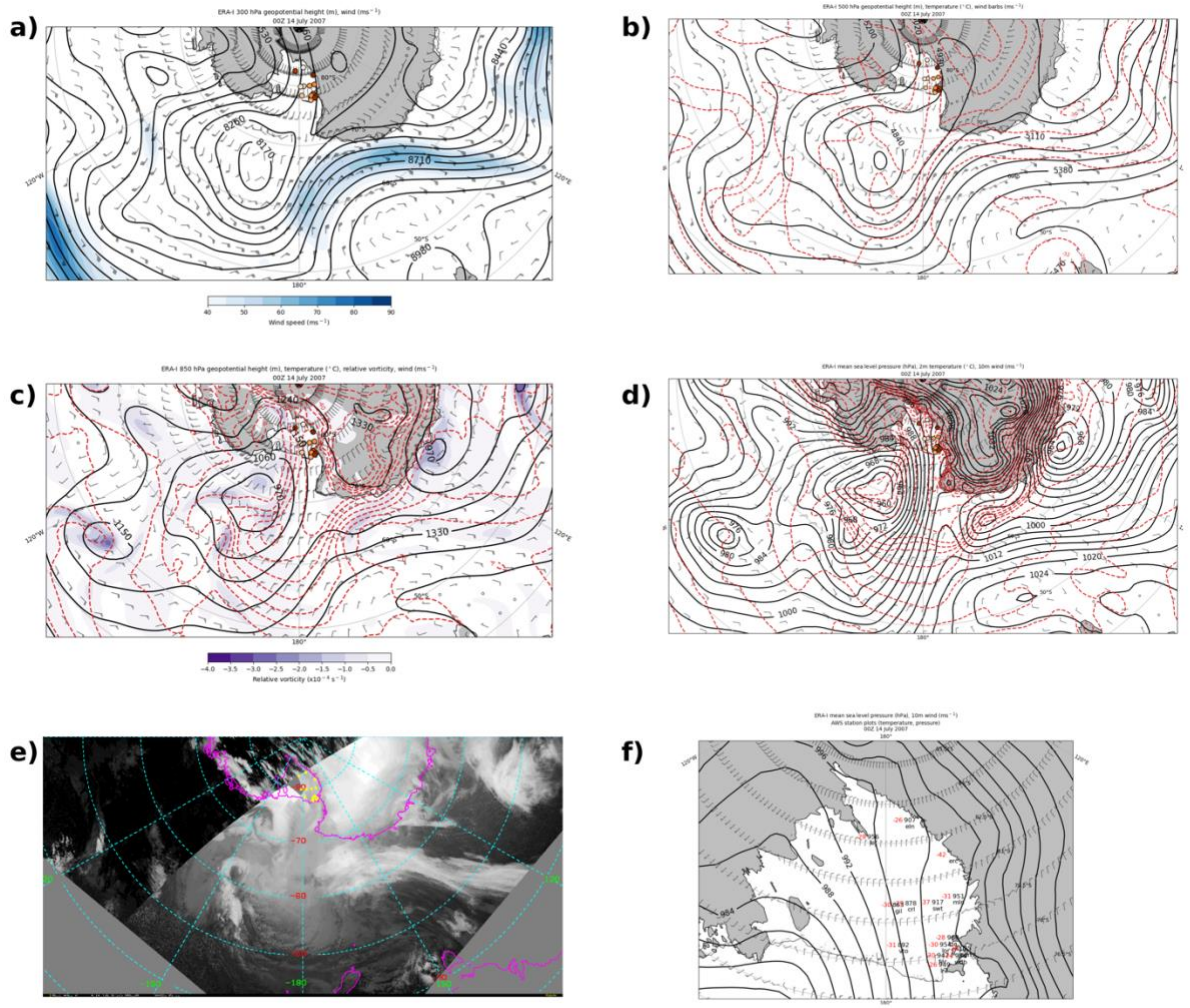

Figure 3.8: As in Fig. 3.3 but for 00 UTC 14 July.

At 12 UTC 14 July, the 300-hPa geopotential height minimum in the Ross Sea progressed eastward and stretched slightly southward as the upstream ridge and wind speed maximum progressed further eastward into the northern Ross Sea (Fig. 3.9a). The ridge downstream shifted eastward while the crest of the ridge progressed poleward, with the wind field over West Antarctica and the RIS maintaining a similar pattern to that of 12 hours prior. The geopotential height minimum at 500 hPa maintained its strength while moving eastward and slightly elongating southward (Fig. 3.9b). The ridge upstream over West Antarctica continued to build over the RIS,

with the baroclinic zone progressing westward over East Antarctica and almost completely across the RIS, leaving 500-hPa temperatures over the RIS relatively uniform. The 850-hPa geopotential height minimum remained in the same location while its trough to the south continued westward (Fig. 3.9c). The cyclonic relative vorticity associated with this trough increased in magnitude, and the baroclinic zone progressed approximately halfway across the RIS as the 850-hPa temperature range remained between -12° C and -24° C. The mean sea level pressure minimum split into a dipole (Fig. 3.9d). The southern of the pressure minima remained the same strength as 12 hours prior (sub-960 hPa) and shifted back westward. The trough to its south progressed westward over the southern Ross Sea and northeastern RIS along with the associated baroclinic zone. The 2-m temperatures in the baroclinic zone ranged from -4° C to -20° C, but this temperature gradient decreased towards the southern RIS. The IR satellite composite imagery indicates the southern of the surface lows was less organized than the northern low (Fig. 3.9e). The northern low had a much tighter circulation evident in the cloud signature. The cloud shield from the southern low was spread over the majority of the RIS, as the cloud signature is whiter over the RIS than earlier. With the surface trough axis over the eastern RIS, the 10-m wind directions indicate northerly flow in the far eastern RIS while southerly flow remained in the western RIS (Fig. 3.9f). AWS pressure observations continued to decrease, ranging from the 980s hPa to 970s hPa. All AWS temperature observations increased as Eric, the final AWS to begin its warming event, began warming. AWS temperatures generally ranged from the low -20°s C to the -30°s C, while Elaine was the warmest at -18° C and Eric was the coldest at -40° C.

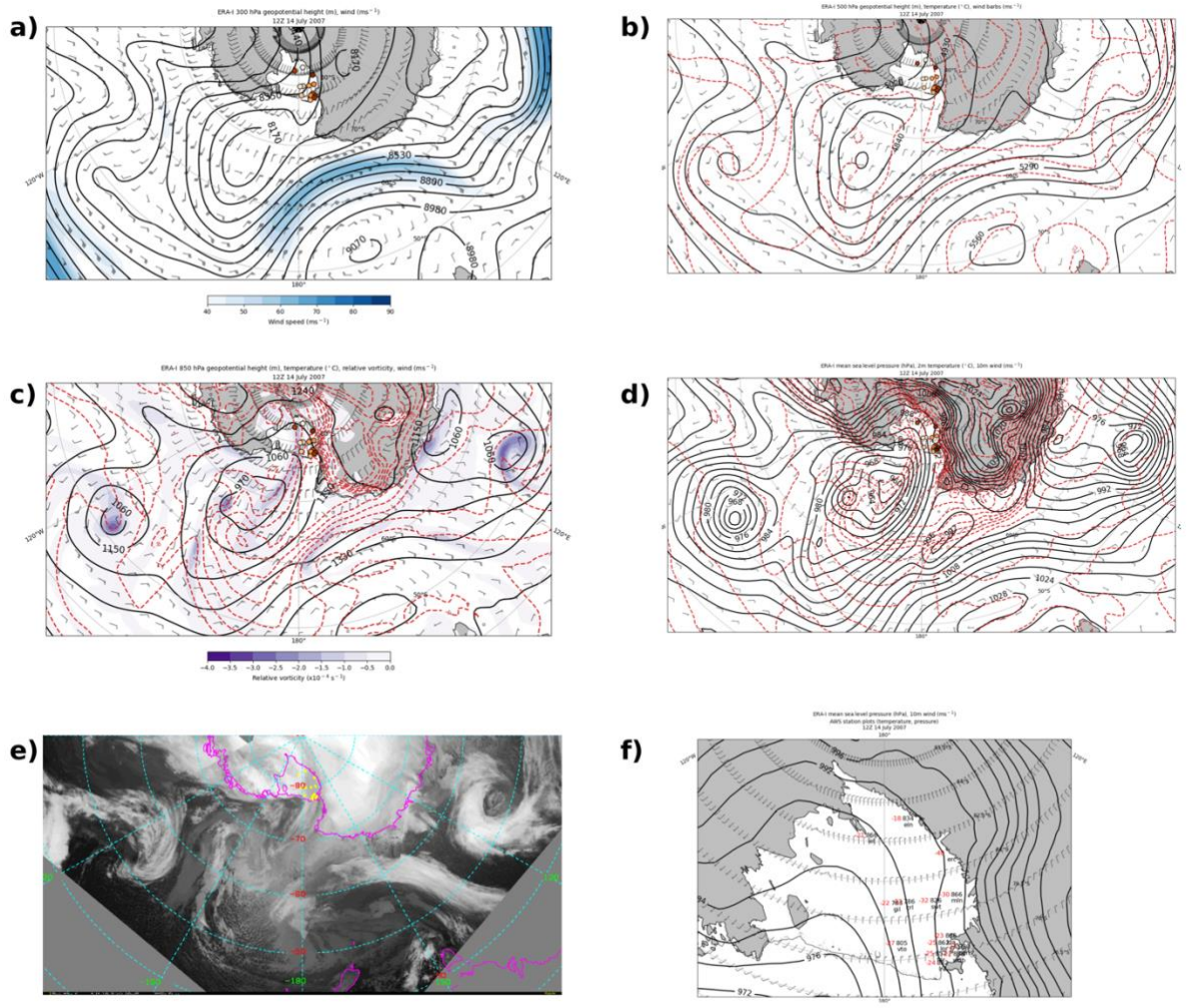

Figure 3.9: As in Fig. 3.3 but for 12 UTC 14 July.

At 00 UTC 15 July, the 300-hPa geopotential height minimum in the southern Ross Sea maintained its strength at sub-8170 m and continued to track southward, with the ridge downstream over West Antarctica maintaining its same approximate position. The jet streak to the northwest of the geopotential height minimum, straddling the Southern Ocean and Ross Sea, became more linear and progressed northeastward. At 500 hPa, the geopotential height minimum in the southern Ross Sea also progressed southward though it elongated and weakened to sub-4840 m. The ridge downstream shifted eastward, and temperatures began to cool over the western RIS, with the

coolest temperatures between -36° C and -40° C. At 850 hPa, the geopotential height minimum maintained its strength at sub-970 m, though the spatial extent of the low decreased. The trough signature to its south became less distinct as it continued westward, reaching the Transantarctic Mountains. The baroclinic zone associated with this trough decreased slightly in magnitude as the cyclonic relative vorticity and temperature gradient both decreased. At the surface, the dipole signature eroded as the primary low remained stationary and weakened to sub-964 hPa while the secondary low to the east progressed southward, now located southeast of the primary low. The warm front and baroclinic zone extending southward from the primary low decreased in magnitude while progressing westward. The 2-m temperatures continued to increase across the RIS, particularly over the north and northwest portions of the RIS. The IR satellite composite imagery indicates distinct cyclonic cloud signatures for the two surface lows. The cloud shield from the primary low still extended south over the RIS, covering essentially the entire ice shelf. The secondary low had a tighter cloud signature as it neared the West Antarctic coast. The surface trough axis progressed westward over the RIS, with northerly 10-m winds to the east and southerly winds to the west. The pressure gradient decreased slightly, notably over the northwestern RIS, decreasing the wind speeds there. AWS pressure observations continued to decrease, ranging from the low 970s hPa to the mid-980s hPa. Each AWS temperature observation increased, though the warming event at Elaine ended late in the day on 14 July.

At 12 UTC 15 July, the 300-hPa geopotential height minimum in the Ross Sea remained at sub-8170 m but decreased in spatial extent as it progressed southward towards the RIS and elongated meridionally (Fig. 3.10a). The ridge downstream progressed eastward, decreasing the geopotential height gradient over the RIS. The jet streak to the north progressed further northeastward into the Ross Sea. At 500 hPa, the geopotential height minimum in the southern

Ross Sea remained at sub-4840 m but decreased in spatial extent as it became further elongated from northeast-to-southwest (Fig. 3.10b). Temperatures continued to cool over the RIS, with temperatures in the eastern RIS reaching colder than -40° C. The disturbance at 850 hPa weakened significantly, as the geopotential height minimum increased to sub-1060 m and covered a large area from the southern Ross Sea to the Amundsen Sea (Fig. 3.10c). The trough over the RIS progressed westward and weakened as the baroclinic zone weakened considerably. There was still a maximum in cyclonic relative vorticity over the northwestern RIS along the Transantarctic Mountains. The surface low in the southern Ross Sea continued weakening to sub-972 hPa, as the secondary low no longer was evident (Fig. 3.10d). The trough progressed further westward almost entirely across the RIS. The associated 2-m temperature gradient continued to weaken, although temperatures increased over the northwestern RIS. The cyclonic cloud signatures in the southern Ross Sea were much less apparent in the IR satellite composite imagery (Fig. 3.10e). The cloud cover over the RIS decreased, with the darker and therefore warmer regions suggesting minimal cloudiness to cloud-free conditions. Some higher clouds remained over the western RIS. With the surface trough progressing westward but weakening, the 10-m winds were northerly in the eastern RIS, easterly in the central RIS, and southerly in the western RIS (Fig. 3.10f). The pressure gradient across the RIS increased slightly, increasing the wind speeds. AWS pressure observations began increasing at most AWS, and AWS temperature observations began to become steady and cool as the warming events ended at Eric, Marilyn, Linda, Lorne, Gill, Ferrell, Lettau, Windless Bight, Vito, Laurie II, Carolyn, and Pegasus North.

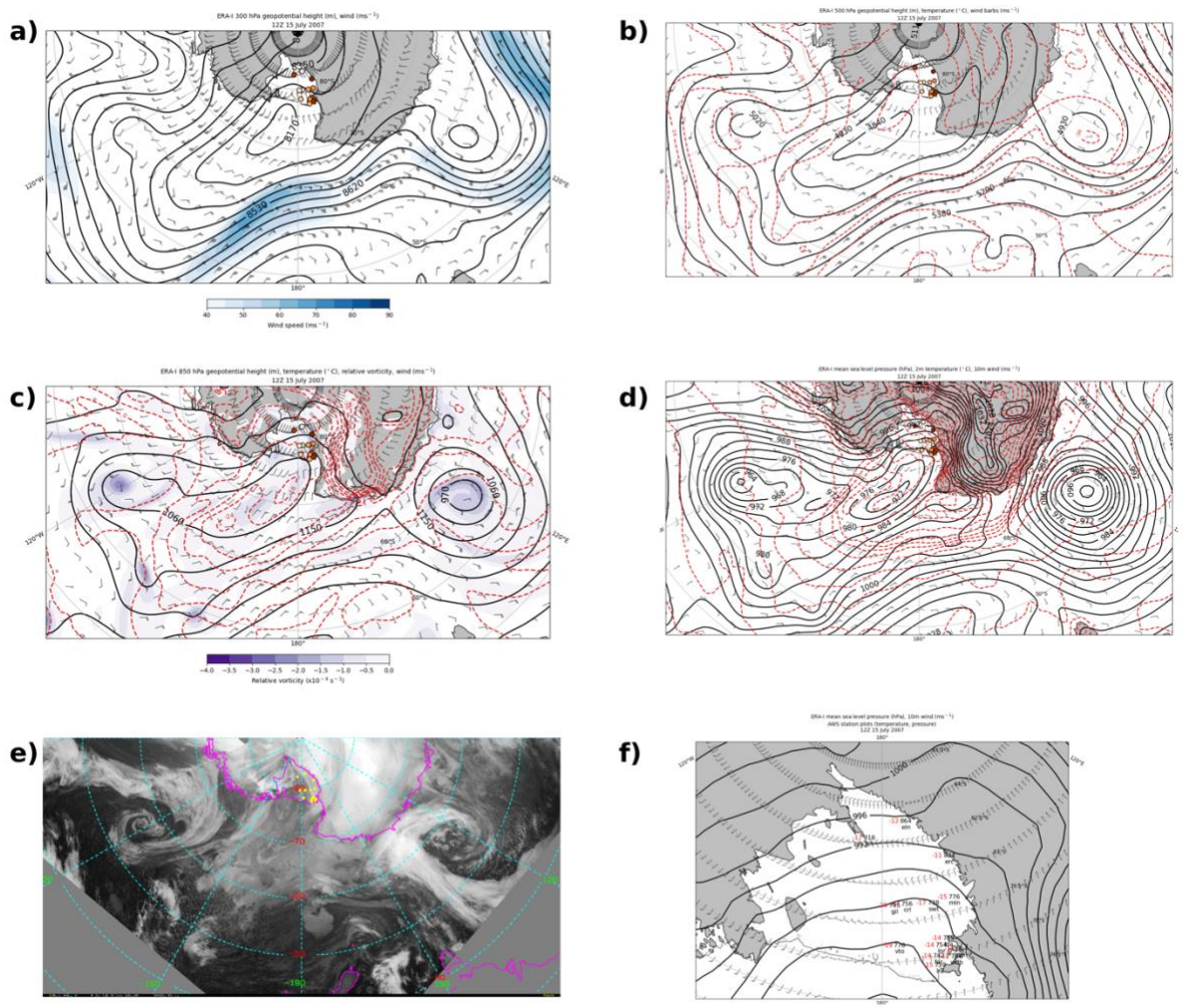

Figure 3.10: As in Fig. 3.3 but for 12 UTC 15 July.

At 00 UTC 16 July, 10 hours and 10 minutes after the final observed warming event ended, in the south-central Ross Sea there were similarly shaped and positioned geopotential height minima at 300 hPa (Fig. 3.11a) and 500 hPa (Fig. 3.11b), while the 850-hPa geopotential height minimum and surface low (Fig. 3.11c, d) were to their east. The 300-hPa geopotential height minimum weakened to sub-8260 m and elongated northeastward (Fig. 3.11a). The geopotential height gradient over the RIS weakened slightly, and the jet streak in the Ross Sea to the north of the geopotential height minimum weakened as it progressed further northeastward. A ridge was

present in the Amundsen Sea and began to reach over West Antarctica. At 500 hPa, the geopotential height minimum in the Ross Sea weakened to sub-4930 m as it elongated like that at 300 hPa (Fig. 3.11b). There was not much variation in temperature over the RIS, and they did not change much from 12 hours prior. There was northerly flow and warm air advection upstream off the coast of West Antarctica. At 850 hPa, the center of the geopotential height minimum shifted eastward into the eastern Ross Sea (Fig. 3.11c). The geopotential height gradient over the RIS weakened slightly, as did the cyclonic relative vorticity near the Transantarctic Mountains. Temperatures remained approximately the same as 12 hours prior. At the surface, the original surface low in the Ross Sea was no longer apparent as a stronger surface low of sub-964 hPa from the northeast in the Amundsen Sea progressed southwest towards the West Antarctic Coast (Fig. 3.11d). This low was located east of the geopotential height minima at 300 and 500 hPa and in the eastern portion of the 850-hPa geopotential height minimum. Over the RIS, the 2-m temperature gradient weakened, with generally warmer temperatures in the northern RIS and cooler temperatures in the southern RIS. The western RIS remained generally cloud-free while high clouds moved over the eastern RIS from the new surface low that had progressed towards the West Antarctic Coast, as the IR satellite composite image shows (Fig. 3.11e). A broad region of cloud cover extended from that surface low over West Antarctica and to the RIS. The AWS pressure observations increased at each site while the trough remained over the western RIS but decreased in spatial extent (Fig. 3.11f). The 10-m winds remained generally northerly to easterly in the eastern and central RIS, respectively, and remained southerly in the western RIS. The AWS temperature observations were the same or colder than 12 hours prior, as the final warming event ended at Schwerdtfeger.

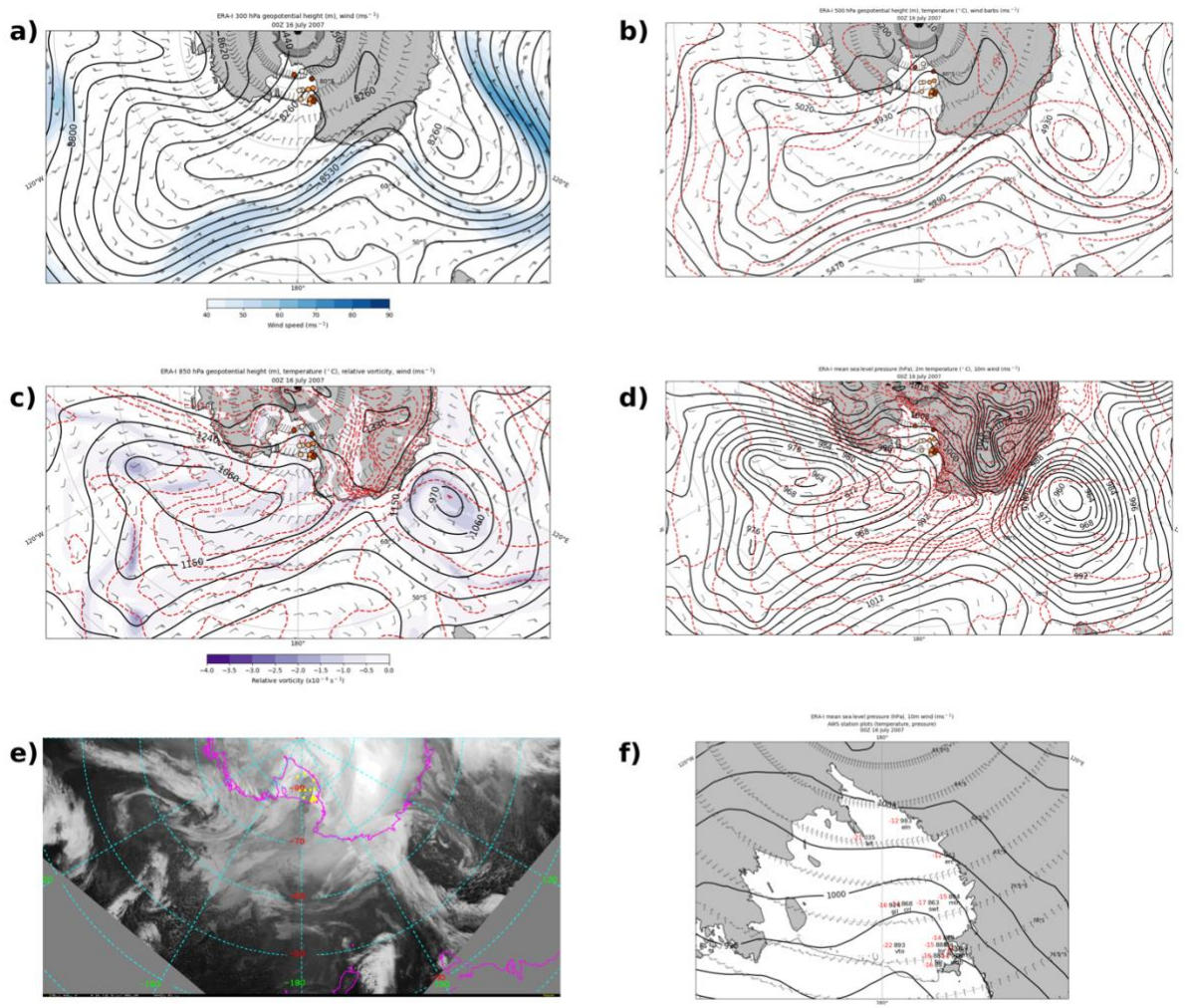

Figure 3.11: As in Fig. 3.3 but for 00 UTC 16 July.

At 12 UTC 16 July, the center of the 300-hPa and 500-hPa geopotential height minima in the Ross Sea shifted north into the middle of the Ross Sea while becoming less elongated. The 850-hPa geopotential height minimum and surface low were both located slightly south of the geopotential height minima at 300 and 500 hPa. At 300 hPa, the geopotential height minimum remained at sub-8260 m while the ridge downstream extended over West Antarctica, positioned to the south of the geopotential height minimum with northerly flow over the RIS. The jet streak on the northwest side of geopotential height minimum extended from the northern Ross Sea to

Cape Adare. The 500-hPa geopotential height minimum deepened to sub-4840 hPa. The ridge to its south, over West Antarctica, brought some warmer air and an increased temperature gradient over the RIS. The temperatures ranged from ~-34° C to ~-42° C, but the gradient magnitude was much weaker than that observed during the warming event. At 850 hPa, the geopotential height minimum in the eastern Ross Sea was stationary and deepened to sub-970 m. There was weak westerly flow to its south over the RIS with a temperature gradient established over the RIS such that warmer temperatures were on the eastern RIS and cooler temperatures on the western RIS. At the surface, the surface low progressed southward as it became zonally elongated. A tight mean sea level pressure gradient was established both to its south, along the West Antarctic Coast, and to its west with strong southerly flow in the western Ross Sea. This led to southerly flow over the RIS, and the 2-m temperature field indicated relatively uniform temperatures across the RIS. The IR satellite composite imagery shows expansive cloudiness stretched from the surface low north of the West Antarctic Coast over West Antarctica and the RIS. The lighter gray colors of the cloud cover over the RIS suggests these are mid-level clouds. The 10-m wind field indicated predominantly southerly flow over the RIS. AWS pressure observations increased, ranging from the mid-980s hPa to the mid-1000s hPa. Most AWS temperature observations were cooler than 12 hours prior.

CHAPTER 4: DISCUSSION

There appear to be four main features that led to the RWEW. The first was a stationary low-ridge setup in the Ross and Amundsen Seas prior to the event. This led to persistent warm, poleward flow and extensive cloud cover towards the West Antarctic Coast. The second feature was a cold pool that developed over the RIS before the event started, manifested by calm winds and a strong surface inversion. These first two features led to the establishment of a strong baroclinic zone north of the RIS. The third feature was the eastward progression of a cyclone off the Adelie Land Coast that merged with the existing stationary low in the Ross Sea. This ultimately led to a southward shift of the cyclone towards the RIS. The fourth feature was the progression of the warm front associated with this cyclone across the RIS. This led to the RWEW by way of warm air advection, cloud cover, and increased wind speeds. This chapter will examine these features before, during, and after the RWEW by analyzing composite plots of ERA5 reanalysis data, analyzing cyclogenesis in the Adelie Land Coast region, using CloudSat/CALIPSO satellite data retrievals to verify cloud features and study the effects of the clouds on temperature, and analyzing the AWS observational data. An analysis of vertical temperature profiles of the surface layer of the atmosphere at Elaine AWS will show that an additional warming mechanism, such as warm air advection, was needed in combination with the erosion of the strong surface inversion for this RWEW to occur.

4.1 Before the event

The ERA-Interim 500 hPa 7-11 July composite geopotential height anomalies preceding the RWEW show a pattern resembling a wave train in the Western Hemisphere of the Southern

Ocean, with a low-high-low setup extending from the northern Ross Sea, off the coast of West Antarctica, and into the South Atlantic Ocean east of South America, respectively (Fig. 4.1a). In the Ross Sea, the geopotential height anomaly was more than 150 m below the climatology. The ridge off the coast of West Antarctica was greater than 400 m above the climatology. The strong anomalous 500-hPa ridge in the Amundsen Sea contributed to the northerly surface flow and buildup of anomalously warm 2-m temperatures prior to the RWEW off the West Antarctic Coast while the RIS was free from any major atmospheric disturbances. At the surface, the composite mean sea level pressure field indicates a broad region of low pressure in the northern Ross Sea that was slightly elongated in the north-south direction (Fig. 4.1b). A broad ridge downstream extended eastward along the West Antarctic Coast, where the warmest 2-m temperature anomalies were located. Between the low pressure and ridge, the orientation of the composite 10-m wind barbs shows near-surface northerly flow.

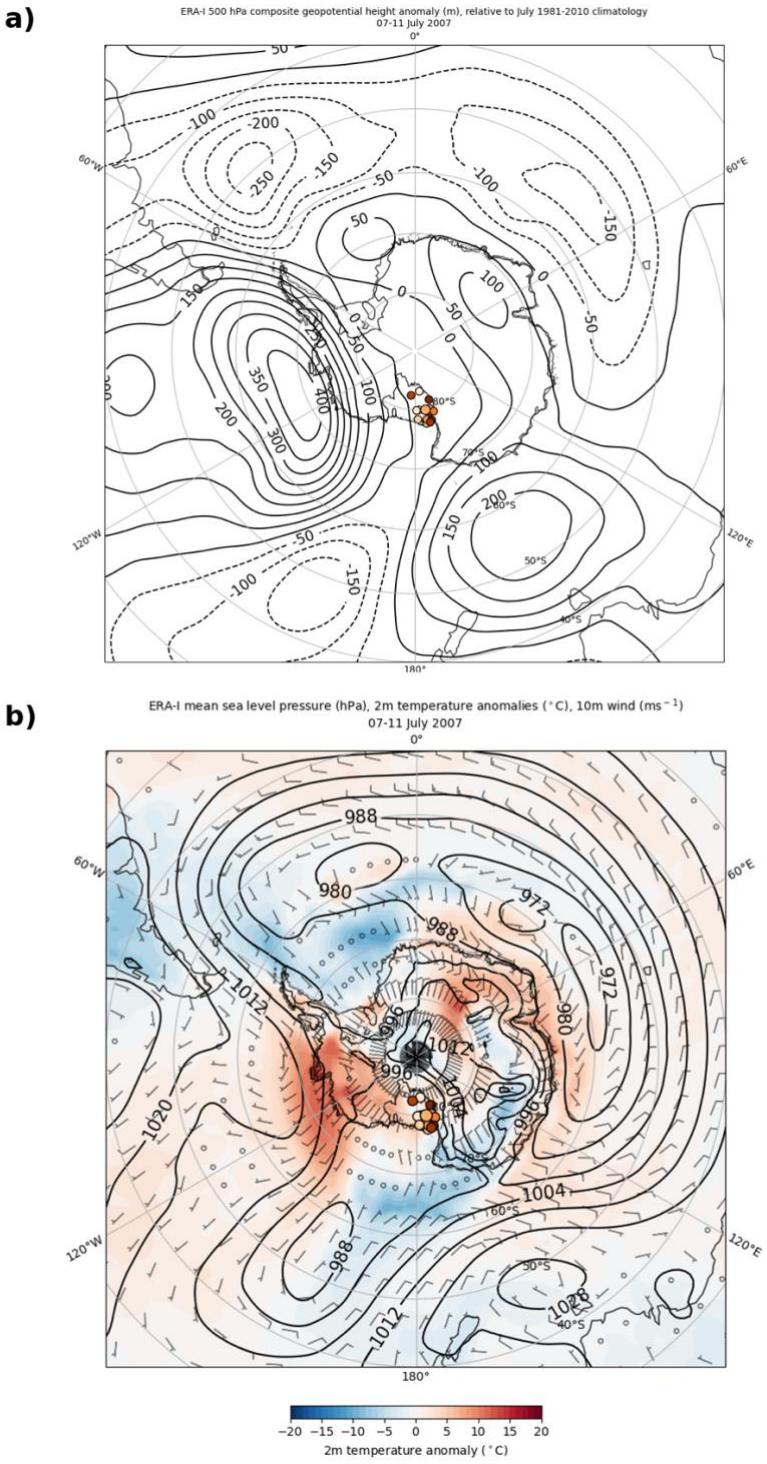

Figure 4.1: ERA-I composite plots from 07-11 July 2007 of a) 500-hPa geopotential height anomalies (m) (black contours, every 50 m, with negative values dashed); b) mean sea level pressure (hPa) (black contours), 2-m temperature anomalies (° C) (color fill), wind barbs (m s^{-1}). Anomalies are relative to the July 1981-2010 climatology. For a) and b), AWS are plotted as in Fig. 3.1a.

The cloud structures varied between the Ross and Amundsen Seas and the RIS two days prior to the beginning of the RWEW, with fog over the open ocean to the north and thin, low clouds to the south over the RIS, both separated by a deep cloud layer. The CloudSat/CALIPSO satellite data retrieval at 09:38:49 UTC 10 July shows the A-train swath extending from 63° S to 81.3° S from the Amundsen Sea, where the ridge was located, southwest over the RIS and over the East Antarctic Plateau (Fig. 4.2a). The cloud phase data retrieval indicates liquid and mixed phase fog and cloud cover in the lowest ~2 km of the atmosphere in the northernmost portion of the retrieval (Fig. 4.2b, panel b), between points A and B, over open ocean water (Fig. 4.2b, panel f). There was a correspondingly strong downwelling longwave radiation (DLR) (Fig. 4.2b, panel c). The warmest ECMWF temperatures of ~270 K were in this location, nearest the surface. A high-altitude ice cloud layer at ~10 km was in the region as well, which can also be seen in lighter grays and white colors in the infrared composite satellite imagery (Fig. 4.3), indicating cold cloud tops, from point A southwestward past point C. This ice cloud layer forms a wedge shape, with a larger spatial extent of cloud cover at the upper levels and a narrower cloud band at the surface between ~64° S and 70° S. This wedge-shaped cloud marks the separation between a warmer air mass to the north and a colder air mass to the south over the RIS, as the ECMWF vertical temperature profile indicates (Fig. 4.2b, panel d). Continuing along the retrieval path over the sea ice to the northeastern edge of the RIS at point D, the cloud phase data indicate mostly low-level ice phase clouds extended from near the surface to ~5 km. There were some areas of near-surface liquid and mixed phase clouds between ~73° S to 75° S. The DLR was weaker in this cloud layer than in the larger wedge-shaped cloud and fog over the open ocean. Over the RIS between points D and E, the low cloud cover thinned even more, as indicated by a smaller region of predominantly ice phase clouds, lower DLR, reflectivity (Fig. 4.2b, panel a), and lower bottom of the atmosphere

longwave cloud radiative effect (BOACRE) values (Fig. 4.2b, panel e) than between points A and C.

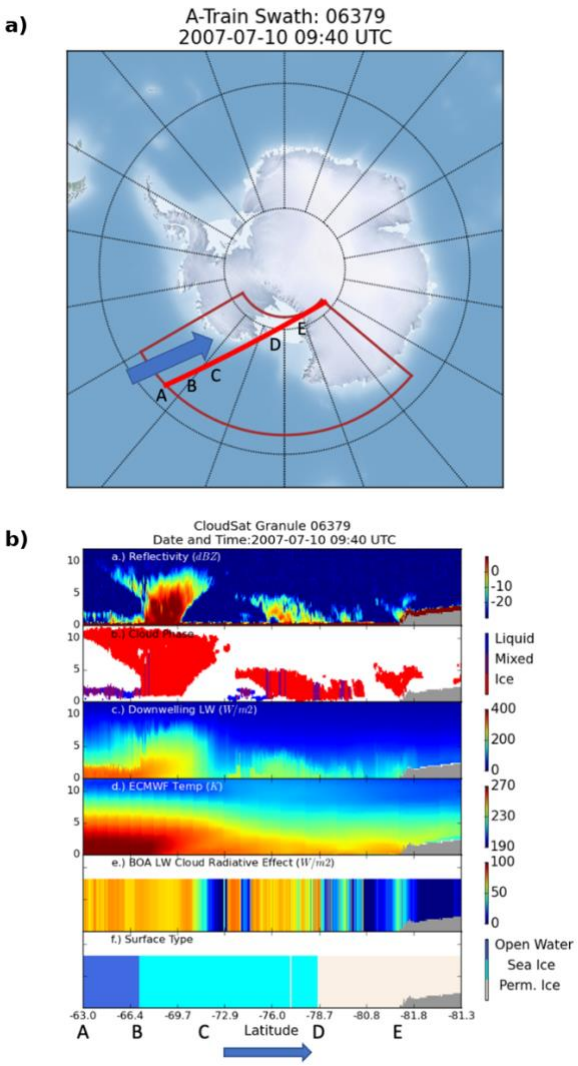

Figure 4.2: CloudSat/CALIPSO A-train satellite constellation data retrievals at 09:40 UTC 10 July 2007. a) The path of the A-train satellite constellation (red) with the blue arrow denoting the direction of travel. Letters correspond to locations discussed in text. b) Panel a) reflectivity (dBZ) from 0 to -30 dBZ; b) Cloud phase: liquid (blue), mixed (purple), ice (red); c) Downwelling longwave radiation (W m^{-2}) from 0 to 400 W m^{-2}; d) ECMWF temperature (K) from 190 to 270 K; e) bottom-of-atmosphere longwave cloud radiative effect (W m^{-2}) from 0 to 100 W m^{-2}; surface type: open water (dark blue), sea ice (light blue), and permanent ice (white). Blue arrow and letters A through E at the bottom correspond to a). The time denotes the time the satellites were at the midpoint of the red line in a).

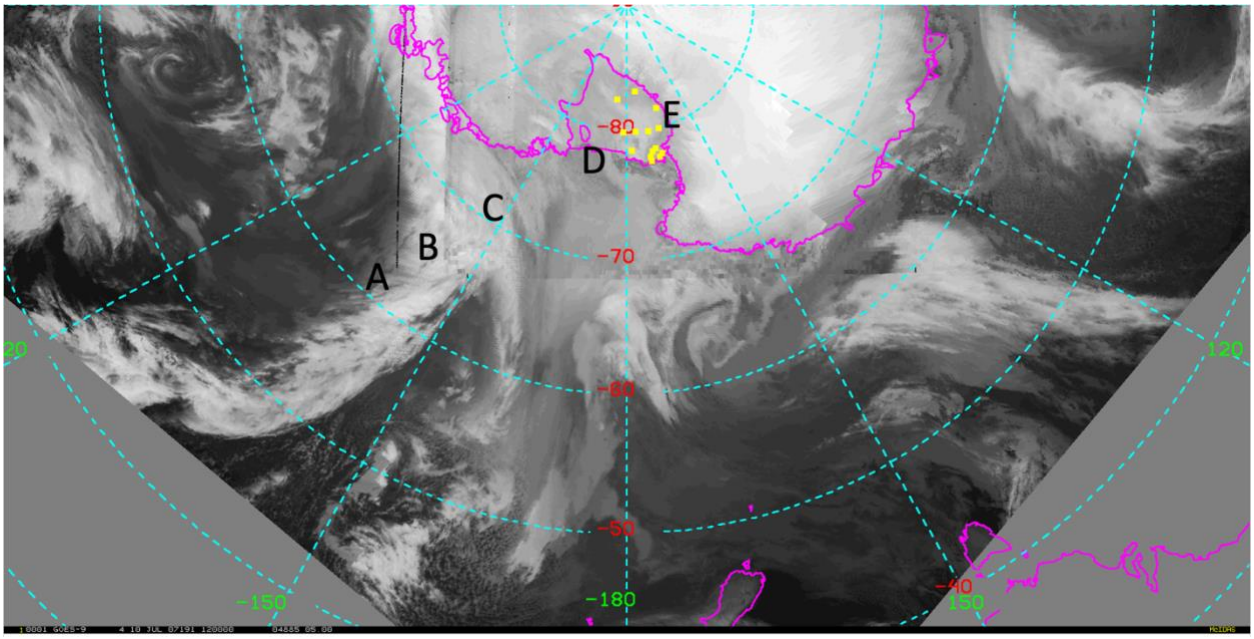

Figure 4.3: Infrared satellite composite image with annotated letters corresponding to locations in Fig. 4.2 and yellow dots denoting AWS locations.

A cold pool developed over the RIS preceding the RWEW. While the 5-day composite 2-m temperature anomalies over the RIS indicated only slightly warm anomalies for this period, the hourly AWS temperature observations (Fig. 4.4) indicate general cooling trends at each location in the two days leading up to the warming events. For most AWS, temperatures trended from near to slightly above the July climatological mean to at least one standard deviation cooler than the mean when the warming event began. In general, wind speeds were calmer in the days leading up to the warming event than during the event (Fig. 4.4). With calm winds, minimal cloud cover as the CloudSat/CALIPSO observations indicate, and no insolation since this is in the middle of austral winter, strong surface temperature inversions developed across the RIS. The 06 UTC 12 July vertical temperature profile at Elaine, the AWS to first begin observing warming, is indicative of this strong inversion (Fig. 4.5). This vertical temperature profile was 10 minutes before the beginning of warming at Elaine, and it shows the steep increase in temperature from the surface to

~975 hPa, followed by a gradual decrease in temperature up to 400 hPa. The ERA-I temperature at 1002 hPa (the surface) was -45.1° C, and at 975 hPa (233 m) it was -28.3° C, a difference of 16.8° C. The magnitude of the warming, according to the Elaine AWS observations, was 39.3° C. Since this is greater than the magnitude of the temperature inversion, this suggests that mixing out of the surface inversion alone would not have been enough to account for all the warming observed.

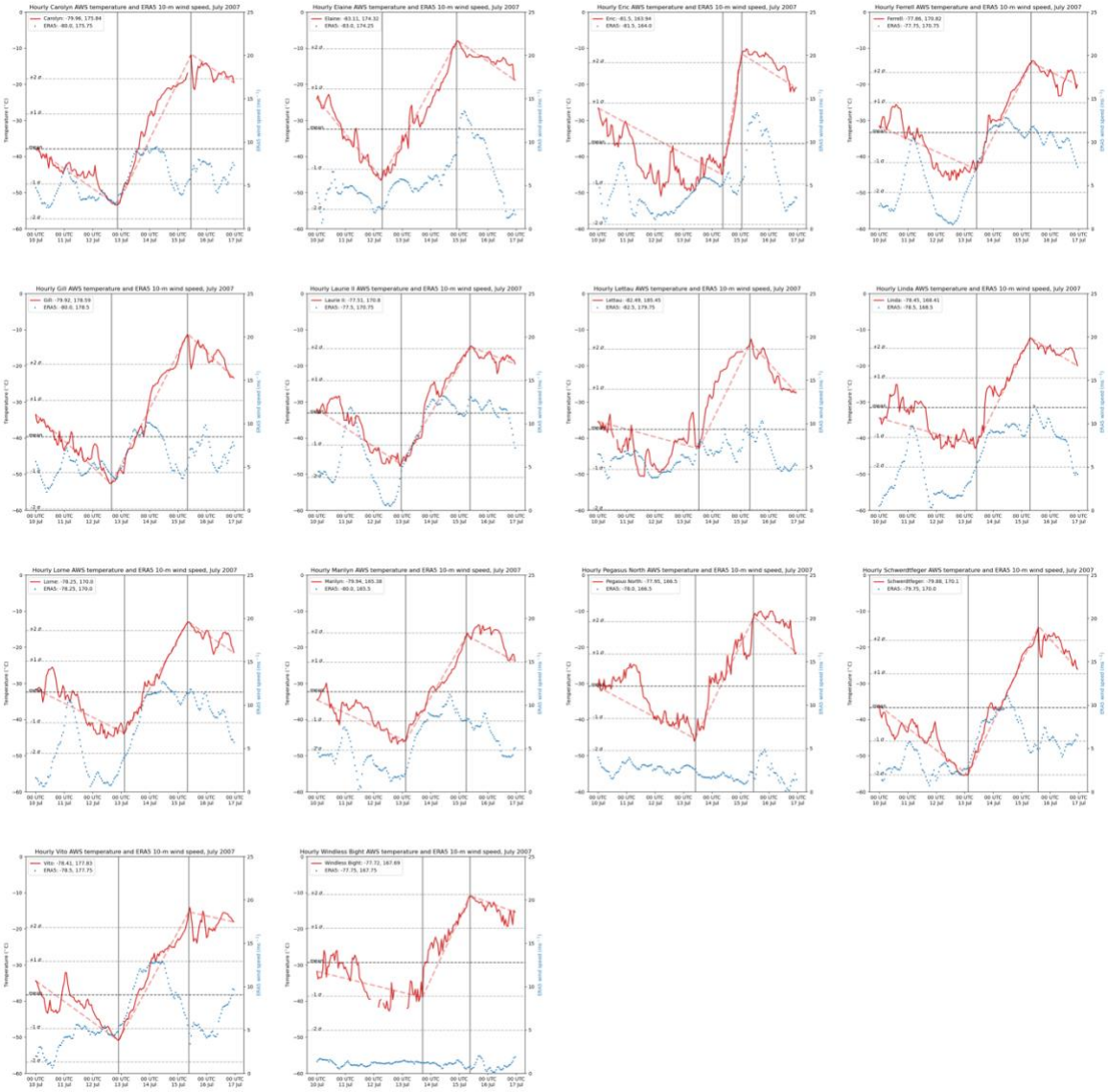

Figure 4.4: As in Fig. 2.1, except blue dots are ERA5 10-m wind speeds (m s^{-1}), and dashed red lines denote the temperature trend before, during, and after each respective warming event.

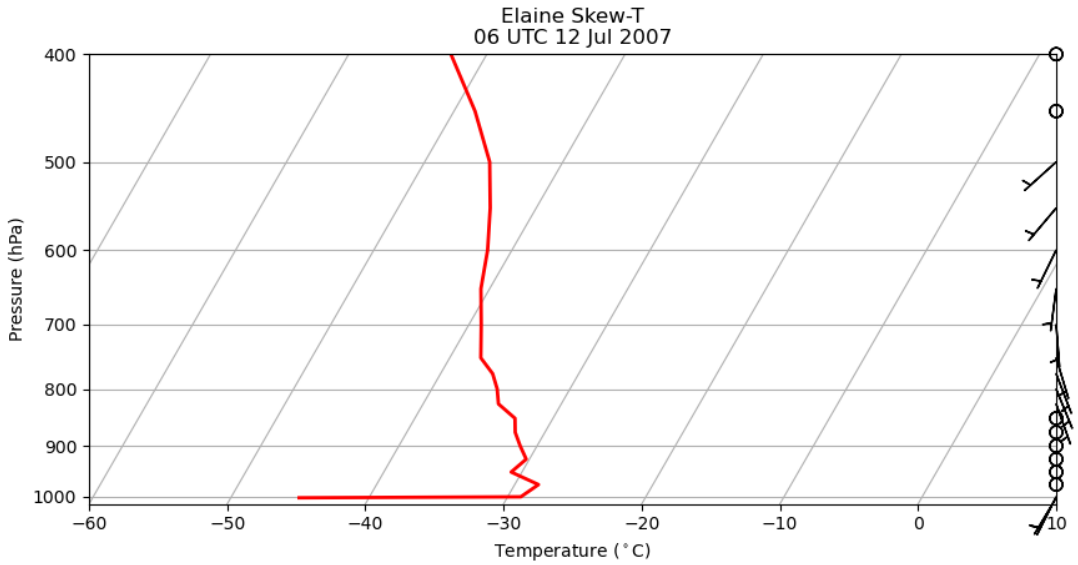

Figure 4.5: ERA-I 06 UTC 12 July 2007 vertical temperature (° C) profile (solid red line) versus pressure (hPa, note the logarithmic scale) and wind barbs (m s^{-1}) at the grid point nearest Elaine (-83.16°, 174.38°).

Upstream of the low in the Ross Sea, two cyclonic disturbances progressed eastward from the Adelie Land Coast and Cape Adare, the first of which being weaker than the second. The first disturbance developed off the Adelie Land Coast between 00 UTC and 06 UTC 10 July, with a central sea level pressure minimum of sub-980 hPa (Fig. 4.6). The 850-hPa relative vorticity minimum associated with this cyclone was displaced slightly westward and upstream from the cyclone center, emblematic of the relatively weak upper-level support. The surface cyclone weakened as it progressed eastward along the near-surface baroclinic zone towards the Ross Sea cyclone. The two cyclones merged between 06 UTC and 12 UTC 11 July, but the near-surface baroclinic zone downstream of the Ross Sea cyclone off the West Antarctic Coast remained stationary (Fig. 3.4c and 3.5c). As the two cyclones merged in the Ross Sea, a surface trough upstream of the Adelie Land Coast progressed southeastward and strengthened into a cyclone off the Adelie Land Coast by 00 UTC 11 July (Fig. 4.7). This disturbance had more upper-level

support, as the 00 UTC 11 July 300- and 500-hPa geopotential heights indicated a deeper collocated trough and the 850-hPa geopotential heights indicated a closed-off circulation (Fig. 3.4a-d). The 850-hPa relative vorticity minimum was much stronger at this time, indicating a well-developed cyclone. While this disturbance progressed eastward off Cape Adare and weakened as it entered the Ross Sea by 12 UTC 12 July (Fig. 3.6), the deeper barotropic support appeared to provide enough energy for it to shift the Ross Sea cyclone southward. This acted to reorient the baroclinic zone meridionally in the southern Ross Sea as the warm front of the Ross Sea cyclone progressed towards the RIS.

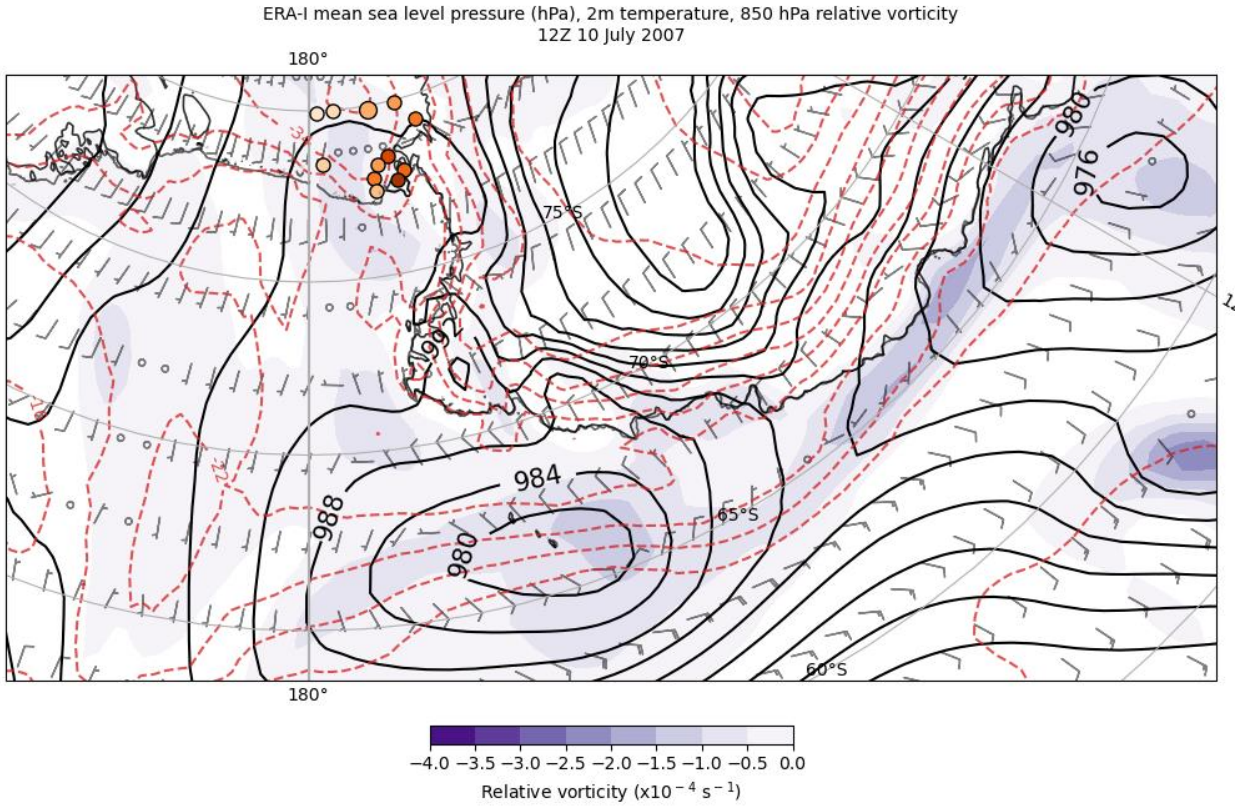

Figure 4.6: ERA-I 12 UTC 10 July 2007 mean sea level pressure (hPa) (black contours), 2-m temperature (° C) (dashed red contours, 850-hPa relative vorticity (10^{-4} s^{-1}) (fill contours from -4 to 0 every 0.5), and 10-m wind barbs (m s^{-1}). AWS are plotted as in Fig. 3.1a.

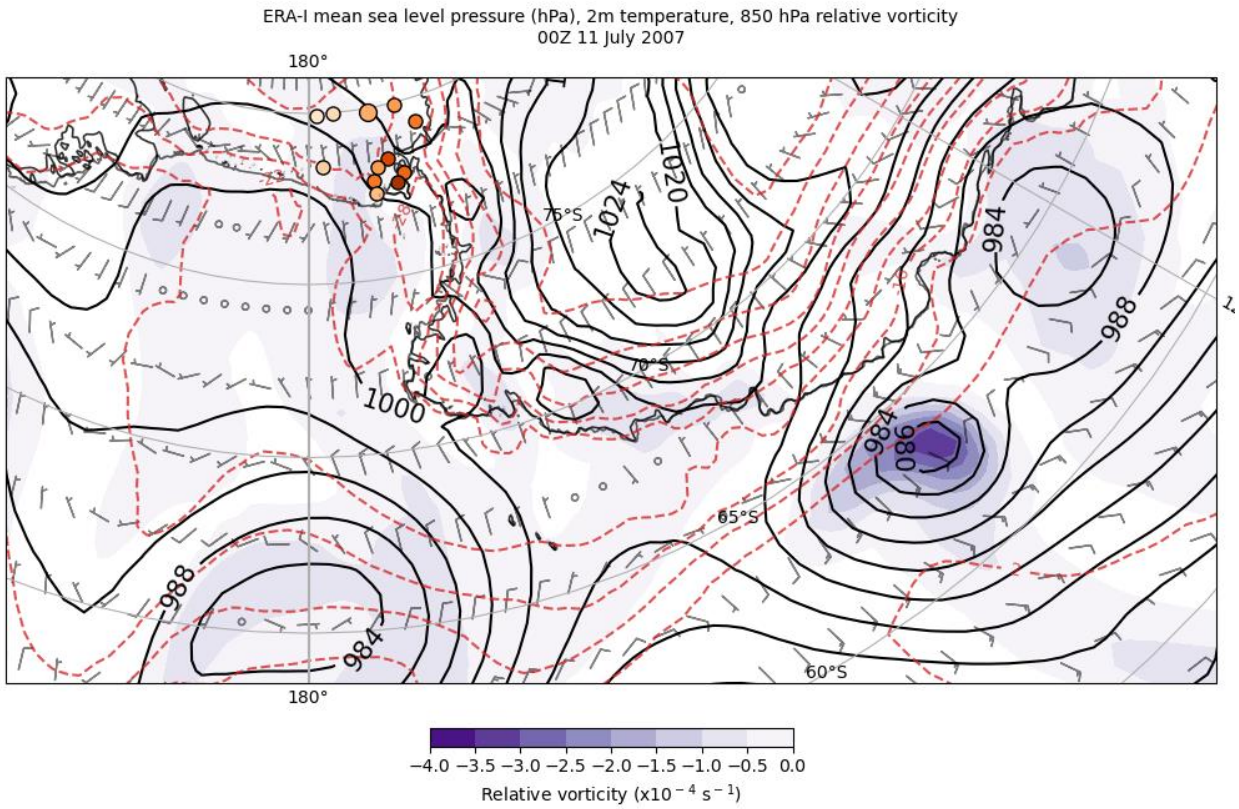

Figure 4.7: As in Fig. 4.6 but for 00 UTC 11 July 2007.

4.2 During the event

During the RWEW (12-15 July), the 500-hPa composite geopotential height anomaly wave train shifted slightly poleward, with the anomalous ridge centered over West Antarctica and the anomalous low in the Ross Sea deepening (Fig. 4.8a). The strength of the geopotential height anomaly in the Ross Sea increased, with values now more than 200 m below the climatology. The anomalous ridge downstream weakened, with maximum values less than 300 m above the climatology. The position of the composite 500-hPa anomalous ridge reflects the ridge building over West Antarctica during the event. At the surface, the composite low shifted southward towards the northeastern edge of the RIS, concentrating the region of anomalously warm 2-m temperatures to West Antarctica and the RIS (Fig. 4.8b). This southward shift reflects the merging

of the existing cyclone in the northern Ross Sea with the cyclone that progressed eastward from the Adelie Land coast and Cape Adare. The shift of the warm 2-m temperature anomalies was an indication of the erosion of the cold pool over the RIS due to the warm frontal passage across the RIS.

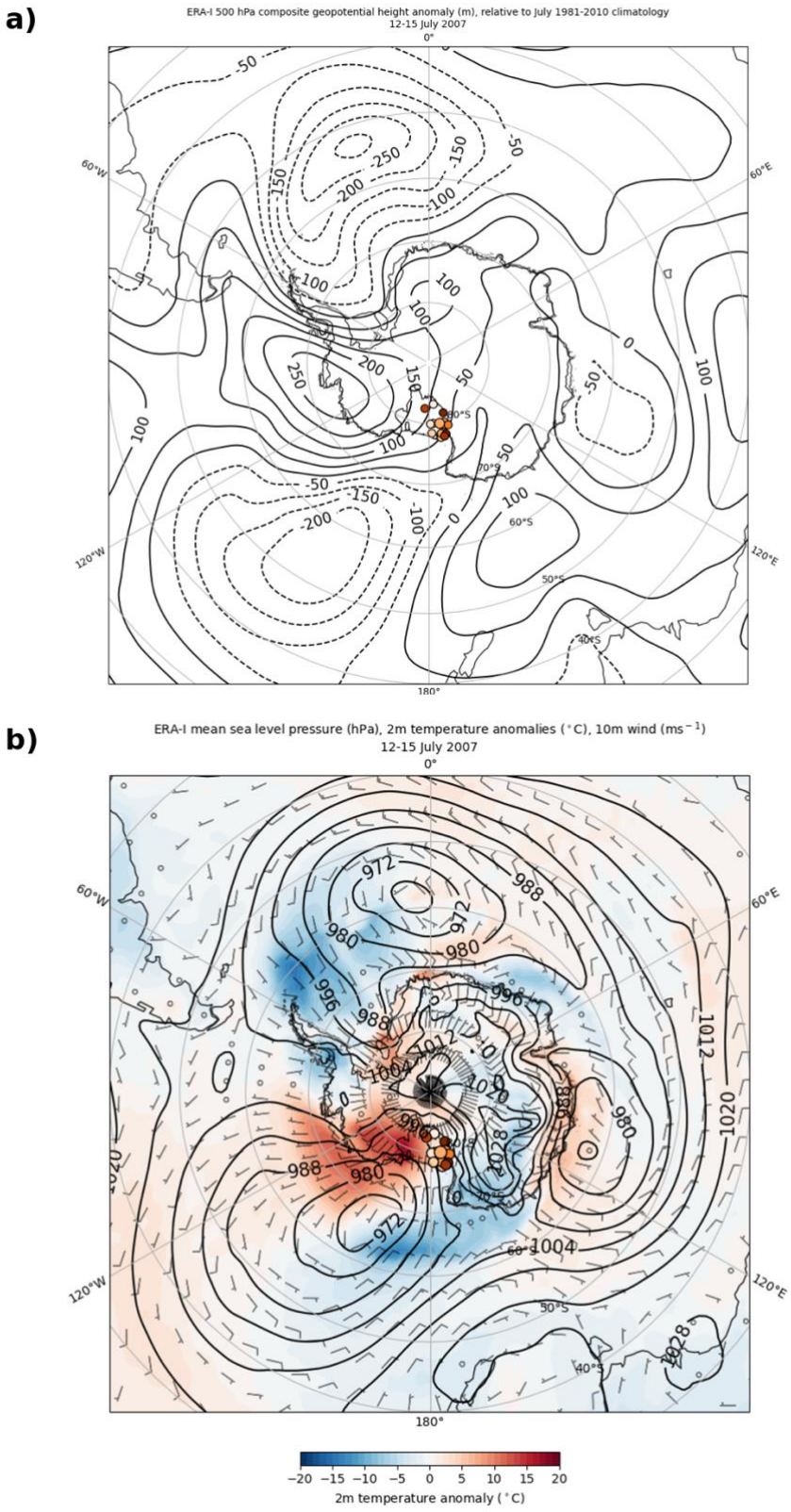

Figure 4.8: As in Fig. 4.1 but for 12-15 July 2007.

A front is characterized as an area with larger-than-background horizontal temperature gradients, larger-than-background relative vorticity, and larger-than-background static stability (Martin 2006). As discussed in Chapter 3, there was a strong horizontal temperature gradient that extended from the surface to 500 hPa and was established north of the RIS preceding the RWEW. On 12 July, when the surface low in the Ross Sea progressed southward towards the RIS, this region of strong temperature contrast began to move across the RIS and was coincident with a local maximum in cyclonic relative vorticity. Figure 4.9 shows the 850-hPa temperature gradient and local minimum in cyclonic relative vorticity associated with the warm frontal passage at 850 hPa across the RIS at 12 UTC 14 July. The region of strongest horizontal temperature gradient over the RIS is collocated and just west, or ahead, of the region of strongest relative vorticity and the trough in geopotential heights. In these terms, the warm front was strongest in the northern RIS, closer to the surface cyclone, compared to the southern RIS at Elaine. The warm frontal signature, however, is still readily evident in the static stability reaching as far south as Elaine. A time-height cross section of ERA5 temperatures at Elaine from 11 July through 16 July illustrates the region of high static stability associated with this warm front (Fig. 4.10). The black vertical lines denote the beginning (06:10 UTC 12 July) and ending (22:10 UTC 14 July) of the warming event observed at Elaine. From 00 UTC 11 July through approximately 06 UTC 12 July, the atmosphere at Elaine from the surface to 400 hPa was well stratified, as indicated by the nearly constant and horizontally oriented isotherms throughout the atmospheric column. After 06 UTC 12 July, the isotherms in the lowest portion of the atmosphere began sloping towards the surface, indicating warming. Between 06 UTC 12 July and 12 UTC 13 July, the isotherms further and further up the atmosphere to 400 hPa began sloping towards the surface, showing warming occurred in more and more of the atmospheric column at Elaine. The sloping bundle of isotherms

marks a region of high static stability, the third characteristic feature of a frontal zone, indicating the presence of a warm frontal passage during this RWEW. The ERA-I 00 UTC 15 July vertical temperature profile at Elaine (Fig. 4.11), just after the warming event ended, also shows warming occurred throughout the atmosphere from the surface to ~400 hPa. The ERA-I temperature at 981 hPa (the surface) warmed from -45.1° C to -12.9° C, an increase of 32.2° C. At 975 hPa (87 m) it warmed from -28.3° C to -8.5° C, an increase of 19.8° C. The magnitude of the surface inversion from the surface to 975 hPa greatly decreased to 4.4° C. Additionally, the wind barbs indicate increased wind speeds at Elaine throughout the entire column. Wind directions ranged from southeasterly at the surface to east-northeasterly at 400 hPa (backing with height), indicative of warm air advection in the Southern Hemisphere. Given this warm frontal signature is evident in the vertical temperature profile at Elaine and the warm frontal signature at 850 hPa is even more pronounced towards the northern RIS, it can be presumed that an equal or greater magnitude warm frontal signature occurred with this RWEW.

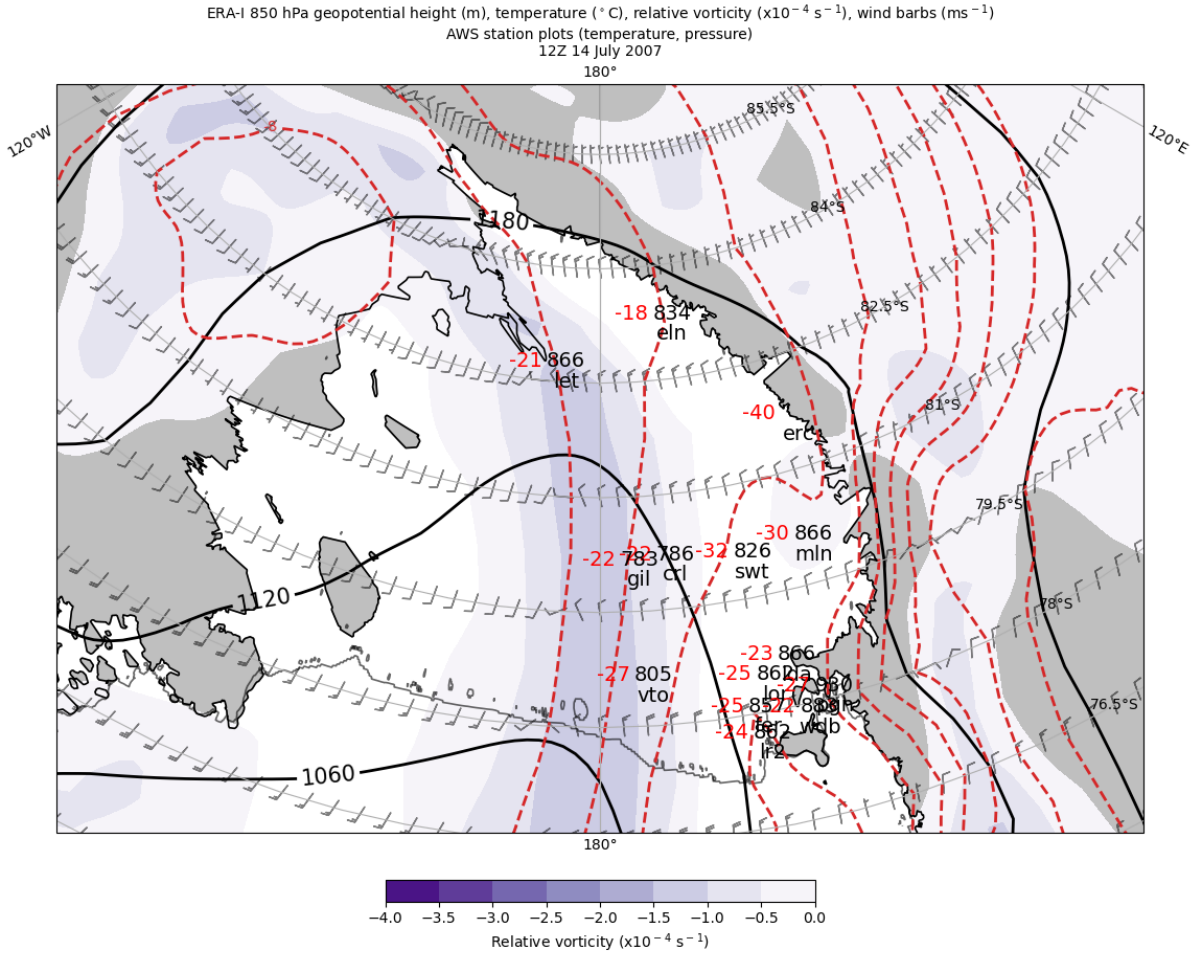

Figure 4.9: ERA-I 12 UTC 14 July geopotential height (m) (black contours), temperature (° C) (dashed red contours), relative vorticity (10^{-4} s^{-1}) (fill contours from -4 to 0 every 0.5), and wind barbs (m s^{-1}).

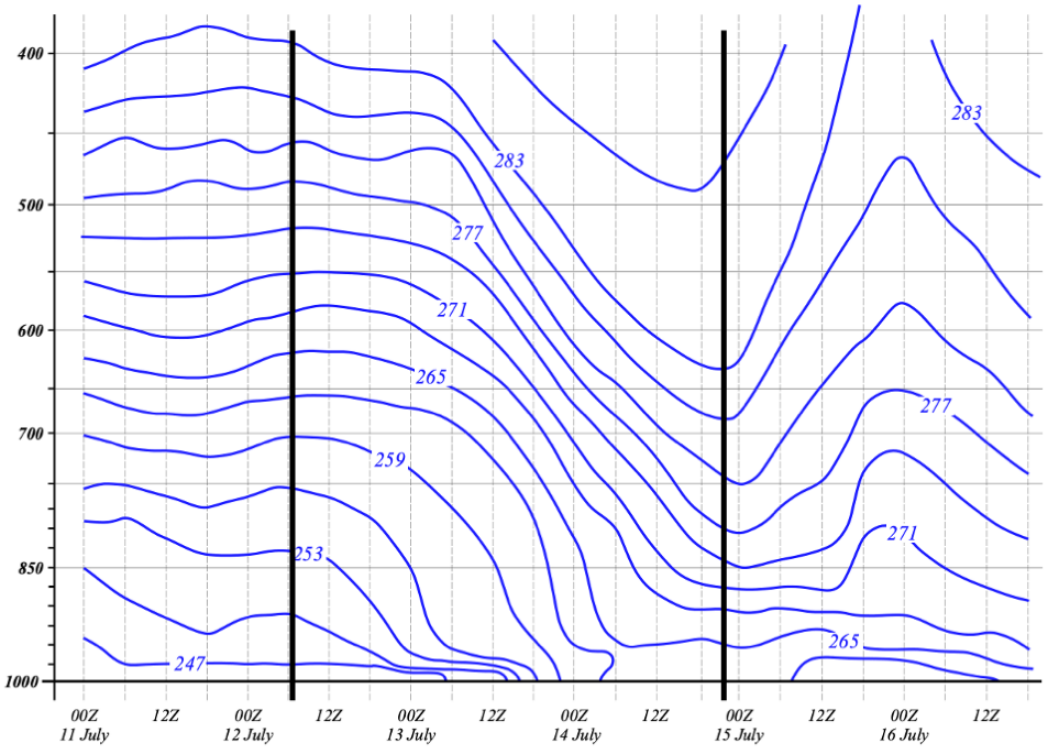

Figure 4.10: ERA5 time versus pressure (hPa, note the logarithmic scale) of temperature (K) (blue contours) at the grid point nearest Elaine. Black vertical lines denote beginning and ending of warming event.

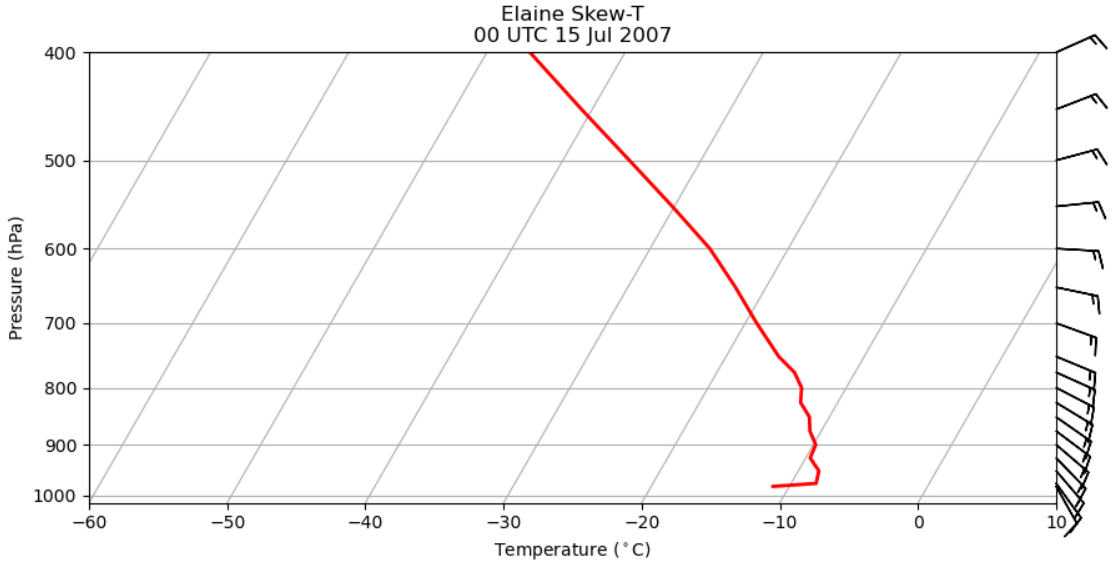

Figure 4.11: As in Fig. 4.5 but for 00 UTC 15 July 2007.

In addition to warm air advection due to the warm frontal passage, another factor that may have led to the erosion of the cold pool and the RWEW was the cloud cover associated with the warm front. As discussed in Chapter 3 and indicated in the IR satellite composite imagery, the approaching surface cyclone brought cloud cover over the RIS from 00 UTC 13 July through 12 UTC 15 July (Figs. 3.7e-3.10e). The Cloudsat/CALIPSO satellite pass over the RIS (Fig. 4.12a) at 07:37 UTC 14 July extended from West Antarctica (between points A and B), over the RIS (between points B and C), and over East Antarctica (between points C and D). High reflectivity values (Fig. 4.12b, panel a) were in the middle of the RIS, ahead of the warm front. The cloud phase (Fig. 4.12b, panel b) indicates ice-phase clouds at or near 10 km covered the majority of the RIS. Low, near-surface cloud cover was over most of the central and west-central RIS. The IR satellite composite image at 06 UTC 14 July confirms the cloud cover, particularly the brighter white signature indicating high clouds over the eastern RIS (Fig. 4.13). Large BOACRE values (Fig. 4.12b, panel e) were coincident with the low cloud cover and higher downwelling longwave radiation near the surface (Fig. 4.12b, panel c), suggesting that high clouds had minimal impact on warming the surface while the low clouds more effectively trapped radiation at the surface. The ECMWF temperature profile (Fig. 4.12b, panel d) indicates much of the atmosphere from the surface to 5 km had warmed over the RIS compared to before the event began (Fig. 4.12b, panel d), with the warmest values just above the surface over the eastern RIS near point B.

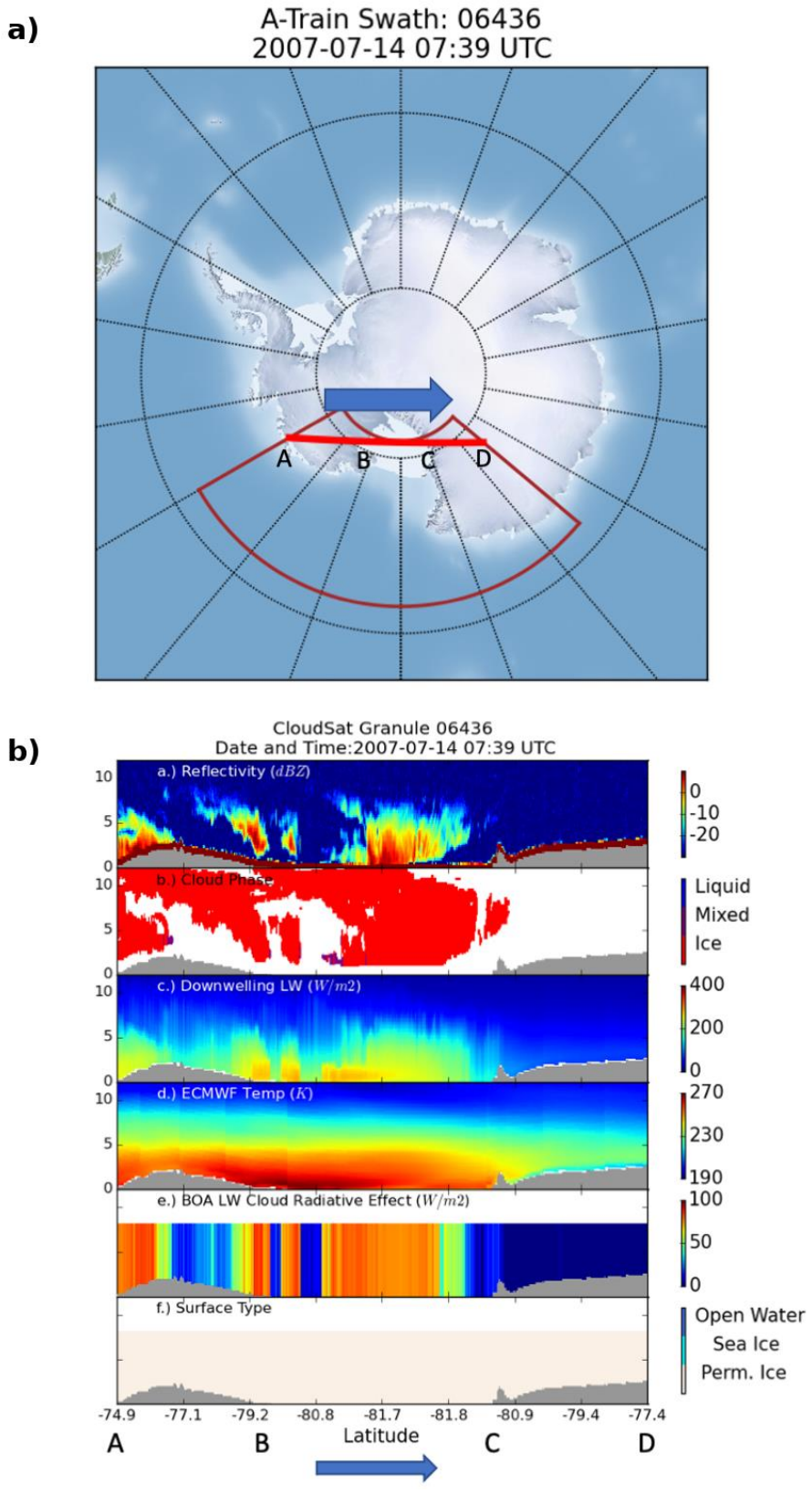

Figure 4.12: As in Fig. 4.2 but for 07:39 UTC 14 July 2007.

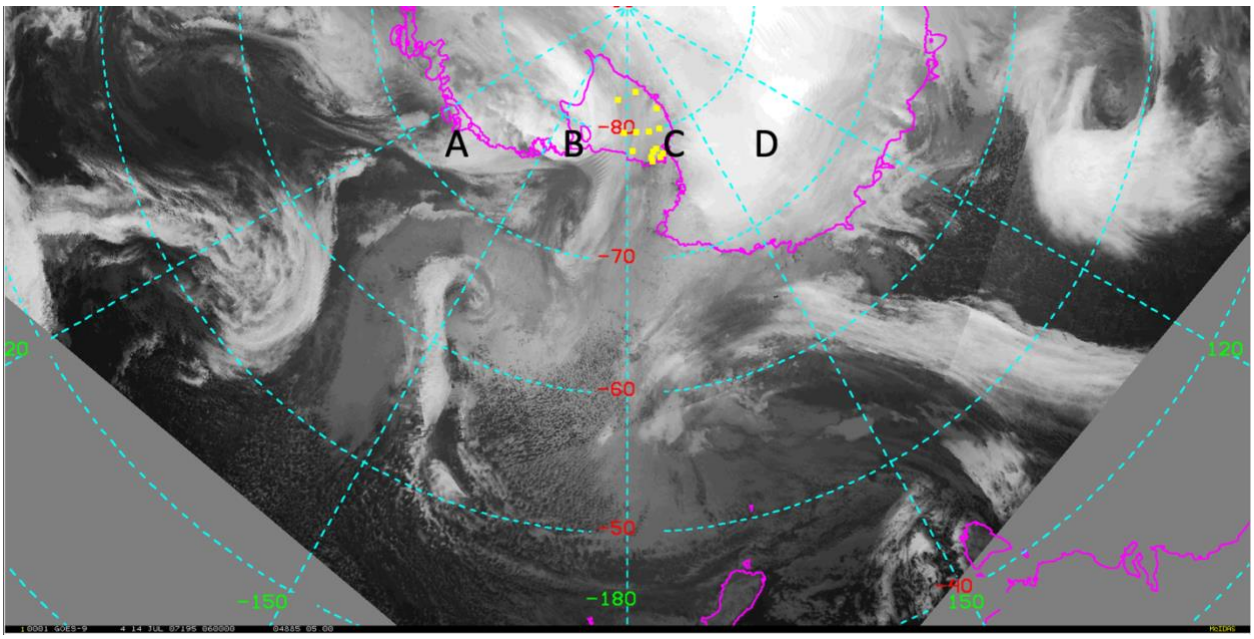

Figure 4.13: As in Fig. 4.3 but for 06 UTC 14 July 2007.

The increased wind speeds and variability in wind speed behavior across the RIS may suggest varying mechanisms contributed to the RWEW, including an increase in wind speed over the RIS. Comparing the wind speeds at Elaine (southern RIS) and Vito (northern RIS), an increase in 10-m winds at both locations coincided with the beginning of the warming (Fig. 4.4). This is consistent with the approach and passage of the warm front; the increased cyclonic vorticity characteristic of the front led to increased wind speeds and warming temperatures. Once the front passed, 10-m wind speeds plateaued at both locations in the middle of the warming, suggesting that a combination of warm air advection and turbulent mixing out of the surface inversion contributed to the beginning of the RWEW. The cloud cover and its longwave radiative feedback further contributed to, and may have sustained, the warming for the latter half of the RWEW as the wind speeds plateaued, though warm air advection was not precluded from continuing in the face of constant wind speeds. Towards the end of the RWEW, at Elaine, wind speeds increased,

reaching a maximum after the warming event ended. At Vito, wind speeds decreased towards the end of the event. This suggests that the approaching cyclone in the Ross Sea amplified the Ross Air Stream (RAS) (Parish et al. 2006, Seefeldt and Cassano 2008), a climatological wind regime observed along the Transantarctic Mountains and originating near Elaine. The wind direction observations at most AWS were more constant compared to their respective climatological means. Figure 4.14 shows Schwerdtfeger wind observations, comparing those during its warming event (Fig. 4.14a) to its July 1991-2020 climatology (Fig. 4.14b). During its warming event, while the prevalent wind direction (west-southwest) did not change, a much larger percentage of wind observations (~70%) were from that direction compared to the climatology (~22%). As discussed in Chapter 2, synoptic-scale cyclones were found to enhance the RAS by increasing the pressure gradient. As shown in Chapter 3, the mean sea level pressure gradient over the RIS was weak before the RWEW, and it increased as the cyclone approached and the warm front progressed across the RIS (Figs. 3.3f-3.11f). The RAS has been found to be most prevalent during winter months, and it may be that its enhancement and sustenance occurs in conjunction with rapid surface warming events such as this RWEW.

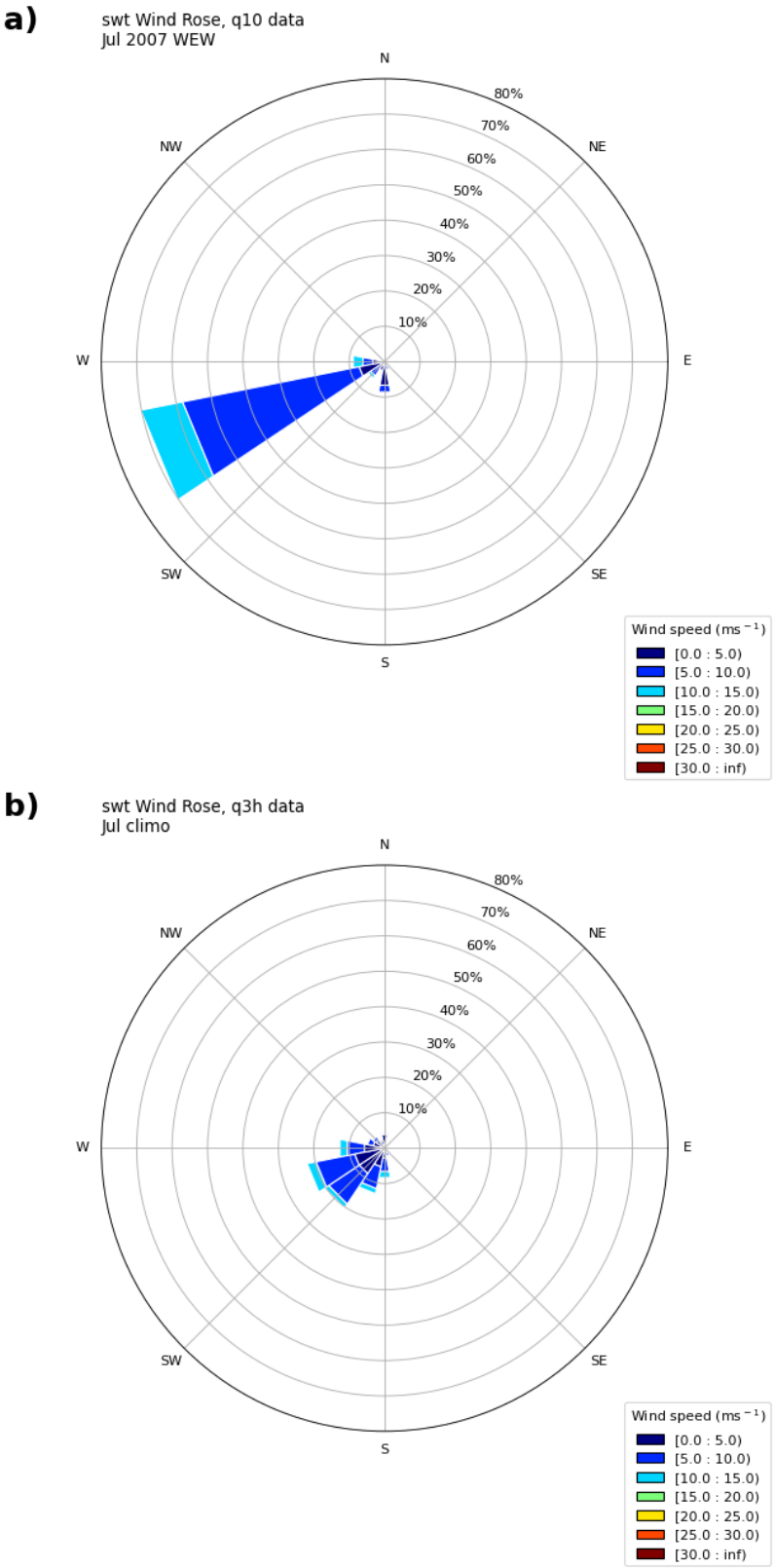

Figure 4.14: Schwerdtfeger wind rose plots a) during the warming event and b) for its July 1991-2020 climatology.

4.3 After the event

After the event (16-20 July), the 500-hPa composite geopotential height anomalies no longer indicated a wave train but rather a meridionally-oriented dipole, with a broad region of anomalously high heights over the RIS and West Antarctica and a similarly intense anomalous low located in the Ross Sea (greater than 250 m below climatology) (Fig. 4.15a). At the surface, the warm 2-m temperature anomalies were not as large in magnitude as during the RWEW but remained over the RIS, West Antarctica, and just north of the RIS in the Ross Sea (Fig. 4.15b). The surface low was now over a broad area in the Amundsen Sea. Since this is a composite plot, this reflects the dissipation and northeastward progression of the surface low near the RIS as it merged with a surface low in the Amundsen Sea. The atmosphere over the RIS became calm as disturbances moved out of the region, leaving the AWS temperatures to resume the general cooling trend that had been observed before the warming event began (Fig. 4.4).

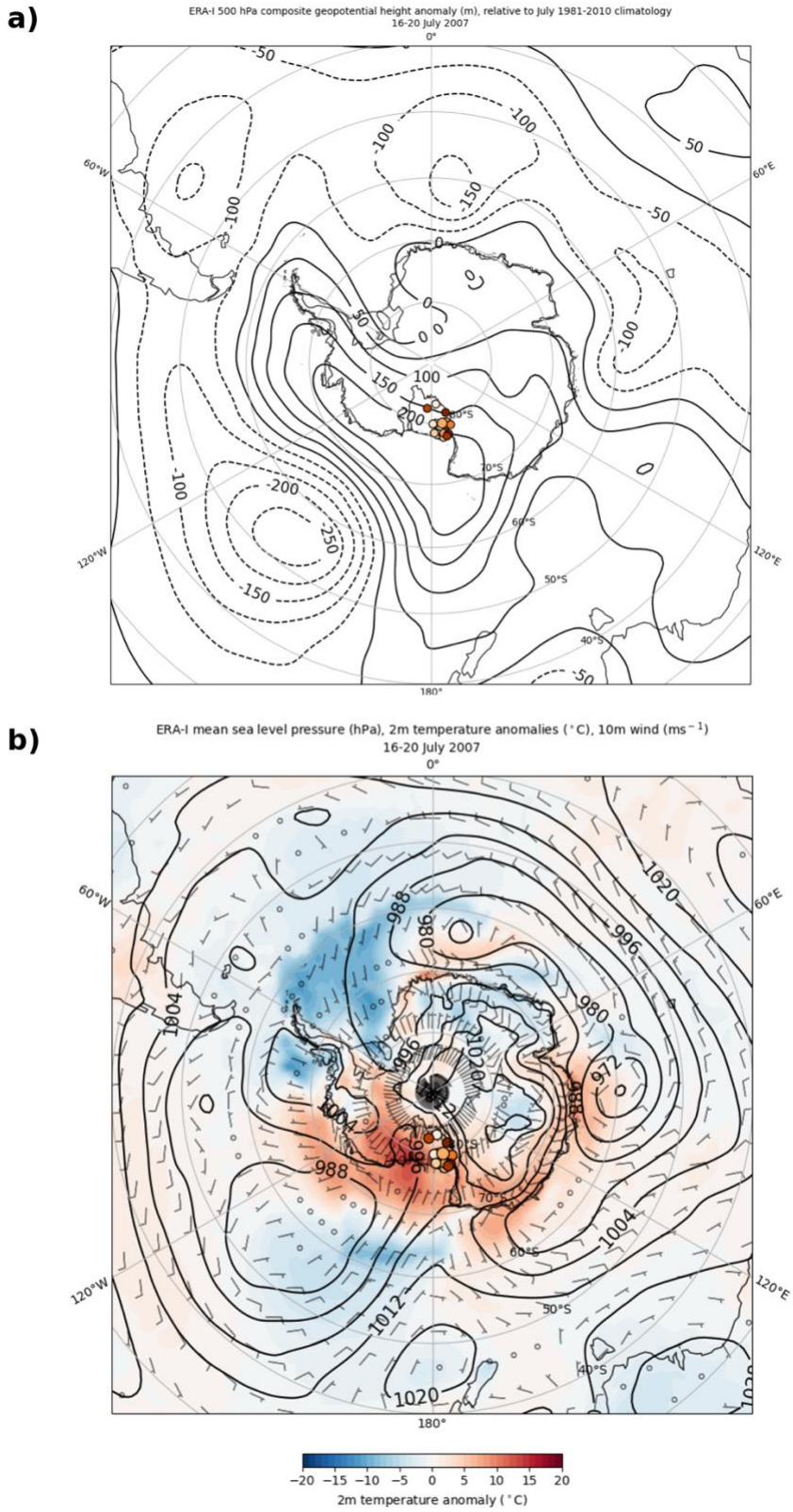

Figure 4.15: As in Fig. 4.1 but for 16-20 July 2007.

CHAPTER 5: CONCLUSION AND FUTURE WORK

This study investigated a Regional Warming Event in Winter (RWEW) that occurred from 12-15 July 2007 and was observed by the University of Wisconsin-Madison (UW-Madison) Automatic Weather Station (AWS) network. A total of 14 AWS observed warming during this RWEW, with the first AWS (Elaine) observing warming at 06:10 UTC 12 July and the last warming ending at Schwerdtfeger at 13:50 UTC 15 July. Using ERA-Interim and ERA5 reanalysis data, satellite composite imagery, CloudSat/CALIPSO satellite data retrievals, and AWS observations, this study investigated the synoptic-scale setup preceding, during, and after the RWEW to determine the large-scale meteorological factors that led to the RWEW. It was found that the passage of a warm front across the RIS from an approaching cyclone in the Ross Sea eroded the cold pool that developed over the RIS and led to the RWEW.

In the days leading up to the RWEW, a 500-hPa wave-train pattern of a geopotential height minimum in the northern Ross Sea and a ridge downstream in the Amundsen Sea led to persistent, northerly flow and buildup of anomalously warm 2-m temperatures off the coast of West Antarctica, north of the RIS. The location of the associated surface cyclone in the northern Ross Sea was a typical positioning of the climatological low known as the Amundsen Sea Low (or Amundsen-Bellingshausen Seas Low) (Turner et al. 2013, Hosking et al. 2013). Over the RIS, calm atmospheric conditions and minimal cloud cover led to the development of a cold pool, with AWS temperatures cooling to greater than one standard deviation below their climatological means. Strong surface temperature inversions occurred, with some inversions reaching 20° C from the surface to 975 hPa. A strong baroclinic zone developed off the West Antarctic Coast between the regions of warm and cold air. Upstream of the Ross Sea cyclone, two cyclones developed off

the Adelie Land Coast, a region with known cyclogenesis (Bromwich et al. 2011), and progressed eastward. The first cyclone had minimal upper-level support and weakened as it entered the Ross Sea. The second cyclone had more substantial upper-level support. It maintained its strength for longer as it progressed eastward into the Ross Sea. It merged with the stationary Ross Sea cyclone, after which the Ross Sea cyclone strengthened and progressed southward towards the RIS. A warm front then developed on the southern portion of the cyclone, with the preestablished baroclinic zone progressing across the RIS from east to west. The RWEW began shortly after the merging of the two cyclones in the Ross Sea, as the progression of the warm front brought with it increased winds and cloud cover over the RIS.

The mechanisms for surface warming were investigated. The warm frontal signature was found to reach as far south as Elaine, spanning the entire RIS. Turbulent mixing, warm air advection, and longwave radiative heating due to cloud cover, acting in concert, were the culprits in generating surface warming of this magnitude. One important finding was that the strength of the surface inversions leading up to the RWEW did not exceed 30° C. Therefore, mixing out of the surface inversion alone could not account for all the warming observed in the RWEW. It is likely, however, that turbulent mixing played some role. It was found that, at most AWS, the beginning of the warming event coincided with increasing wind speeds. This suggests some combination of warm air advection and turbulent mixing could have initiated the warming. Cloud cover, however, accompanied the warm front and contributed to an increase in longwave radiation at the surface. This may have contributed to the onset of warming and sustained the warming throughout the event. As the RWEW continued over the RIS, wind speeds at sites in the northern RIS plateaued and decreased while wind speeds at sites in the southern RIS plateaued and increased. This wind pattern also resembles the climatological wind regime over the RIS (Costanza

et al. 2016), with weaker winds in the northern RIS and stronger winds along the Transantarctic Mountains. It is also indicative of the nearby surface cyclone, in turn enhancing the Ross Air Stream (RAS), a climatological wind regime of strong southerly winds along the Transantarctic Mountains (Coggins et al. 2014, Parish et al. 2006, Seefeldt and Cassano 2008).

Future work on this RWEW will investigate how the 500-hPa wave train pattern was established prior to the warming, focusing on tropical teleconnections. Additionally, a more quantitative analysis can better characterize the different warming mechanisms over the RIS, investigating how the increased wind speeds impact the magnitude of warm air advection and turbulent mixing over the RIS. With an enhanced RAS, adiabatic warming due to compression from katabatic winds off the West and East Antarctic Plateaus may also contribute to warming at AWS along the Transantarctic Mountains. The surface energy budget can be further investigated and quantified to determine the magnitude of the longwave radiative feedback due to the cloud cover over the RIS, including the possible latent heat release due to cloud formation. The variation of these warming mechanisms across the RIS may be useful to show how likely such strong and rapid warming events are to occur in the future. This may also provide insights into extreme departures from climatology in austral winter that sometimes occur over other regions in Antarctica.

REFERENCES

Ball, F. K., 1956: The theory of strong katabatic winds. *Aust. J. Phys.,* **9,** 373–386.

Bromwich, D. H., D. F. Steinhoff, I. Simmonds, K. Keay, and R. L. Fogt, 2011: Climatological aspects of cyclogenesis near Adelie Land, Antarctica. *Tellus A: Dynamic Meteorology and Oceanography*, **63:5**, 921-938, DOI: 10.1111/j.1600-0870.2011.00537.x

CloudSat Data Processing Center (DPC), 2022: ECMWF-AUX description, 2022-03-31, 2022, https://www.cloudsat.cira.colostate.edu/data-products/ecmwf-aux.

Coggins, J. H., McDonald, A. J., and Jolly, B., 2014: Synoptic climatology of the Ross Ice Shelf and Ross Sea Region of Antarctica: *k*-means clustering and validation. *Int. J. Climatol.*, **34**, 2330-2348, DOI:10.1002/joc.3842.

Costanza, C., M. Lazzara, L. Keller, and J. Cassano, 2016: The surface climatology of the Ross Ice Shelf Antarctica. *Int. J. Climatol.*, **36**, 4929-4941.

Dee, D. P., S. M. Uppala, A. J. Simmons, P. Berrisford, P. Poli, S. Kobayashi, U. Andrae, M. A. Balmaseda, G. Balsamo, P. Bauer, P. Bechtold, A. C. M. Beljaars, L. van de Berg, J. Bidlot, N. Bormann, C. Delsol, R. Dragani, M. Fuentes, A. J. Geer, L. Haimberger, S. B. Healy, H. Hersbach, E. V. Hólm, L. Isaksen, P. Kållberg, M. Köhler, M. Matricardi, A. P. McNally, B. M. Monge-Sanz, J.-J. Morcrette, B.-K. Park, C. Peubey, P. de Rosnay, C. Tavolato, J.-N. Thépaut, and F. Vitart, 2011: The ERA-Interim reanalysis: configuration and performance of the data assimilation system. *Q.J.R. Meteorol. Soc*., **137**, 553–597, DOI:10.1002/qj.828.

Gossart, A., Helsen, S., Lenaerts, J. T. M., Broucke, S. V., van Lipzig, N. P. M., and Souverijns, N., 2019: An evaluation of surface climatology in state-of-the-art reanalyses over the Antarctic ice sheet, *J. Climate*, **32**, 6899-6915, DOI: 10.1175/JCLI-D-19-0030.1.

Henderson, D. S., L'Ecuyer, T., Stephens, G., Partain, P., & Sekiguchi, M., 2013: A multisensory perspective on the radiative impacts of clouds and aerosols. *J. Appl. Meteor.*, **52**, 853–871. https://doi.org/10.1175/JAMC-D-12-025.1.

Hersback, H., and Coauthors, 2020: The ERA5 global reanalysis, *Quart. J. Roy. Meteor. Soc.*, **146**, 1999-2049, https://doi.org/10.1002/qj.3803.

Hirasawa, N., N. Hisashi, and T. Yamanouchi, 2000: Abrupt changes in meteorological conditions observed at an inland Antarctic station in association with wintertime blocking. *Geophys. Res. Lett.*, **27**, 1911-1914.

Hirasawa, N., H. Nakamura, H. Motoyama, M. Hayashi, and T. Yamanouchi, 2013: The role of synoptic-scale features and advection in prolonged warming and generation of different forms of precipitation at Dome Fuji station, Antarctica, following a prominent blocking event. *J. Geophys. Res. Atmos.*, **118**, 6916-6928, DOI:10.1002/jgrd.50532.

Hosking, J. S., A. Orr, G. J. Marshall, J. Turner, and T. Phillips, 2013: The influence of the Amundsen-Bellingshausen Seas Low on the climate of West Antarctica and its representation in coupled climate model simulations. *J. Climate*, **26**, 6633-6648, DOI:10.1175/JCLI-D-12-00813.1.

Kohrs, R., M. Lazzara, J. Robaidek, D. Santek, S. Knuth, 2013: Global Satellite Composites – 20 Years of Evolution. *J. Atmos. Res.*, **135-136**, 8-34, DOI:10.1016/j.atmosres.2013.07.023.

Lazzara, M. A., J. M. Benson, R. J. Fox, D. J. Laitsch, J. P. Rueden, D. A. Santek, D. M. Wade, T. M. Whittaker, and J. T. Young, 1999: The man computer interactive data access system: 25 years of interactive processing. *Bull. Amer. Meteor. Soc.*, **80**, 271-284, DOI:10.1175/1520-0477(1999)080<0271:TMCIDA>2.0.CO;2.

Lazzara, M., G. Weidner, L. Keller, J. Thom, and J. Cassano, 2012a: Antarctic Automatic Weather Station Program: 30 Years of Polar Observation. *Bull. Amer. Meteor. Soc.*, **93**, 1519-1537.

Lazzara, M. A., L. M. Keller, T. Markle, and J. Gallagher, 2012b: Fifty-year Amundsen-Scott South Pole station surface climatology. *Atmos. Res.*, **118**: 240–259, doi: 10.1016/j.atmosres.2012.06.027.

L'Ecuyer, T. S., and J. H. Jiang, 2010: Touring the atmosphere aboard the A-Train. *Phys. Today*, **63**, 36–41, doi:10.1063/1.3463626.

Marchand, R., Mace, G. G., Ackerman, T., and Stephens, G., 2008: Hydrometeor detection using Cloudsat – An earth-orbiting 94-GHz cloud radar. *J. Atmos. Oceanic Tech.*, **25**, 519–533, https://doi.org/10.1175/2007JTECHA1006.1.

Martin, J. E., 2006: Mid-Latitude Atmospheric Dynamics: a first course.

Parish, T. R. and J. J. Cassano, 2003: The Role of Katabatic Winds on the Antarctic Surface Wind Regime. *Mon. Wea. Rev.*, **131**, 317-333. DOI: https://doi.org/10.1175/1520-0493(2003)131<0137:TROKWO>2.0.CO;2.

Parish, T.R., J. J. Cassano, and M. W. Seefeldt, 2006: Characteristics of the Ross Ice Shelf air stream as depicted in Antarctic Mesoscale Prediction System simulations. *J. Geophys. Res. Atmos.* **111**(D12), DOI: 10.1029/2005JD006185.

Schwerdtfeger, W., 1970: The climate of the Antarctic. Chapter 4 In: Orvig, S. (Ed.), World Survey of Climatology, vol. XIV. Elsevier, Amsterdam, 253–355.

Seefeldt, M. W. and J. J. Cassano, 2008: An Analysis of Low-Level Jets in the Greater Ross Ice Shelf Region Based on Numerical Simulations. *Mon. Wea. Rev.*, **136**, 4188-4205, DOI:10.1175/2008MWR2455.1.

Seefeldt, M. W. and J. J. Cassano, 2012: A description of the Ross Ice Shelf air stream (RAS) through the use of self-organizing maps (SOMs). *J. Geophys. Res. Atmos.* **117**(D09), DOI: 10.1029/2011JD016857.

Tetzner, D., Thomas, E. R., Allen, C. S., 2019: A validation of ERA5 reanalysis data in the southern Antarctic Peninsula-Ellsworth Land region, and its implications for ice core studies. *Geosciences*, **9**, 289, DOI: 10.3390/geosciences9070289.

Thompson, D., 1969: The coreless winter at Scott Base, Antarctica. *Quart. J. R. Met. Soc.*, **95**, 404-407.

van Loon, H., 1967: The Half-Yearly Oscillations in Middle and High Southern Latitudes and the Coreless Winter. *J. Atmos. Sci.*, **24**, 472-486, DOI:10.1175/1520-0496(1967)024<0472:THYOIM>2.0.CO;2.

Wang, Z., Vane, D., and Stephens, G.: Level 2 Combined Radar and Lidar Cloud Scenario Classification Product Process Description and Interface Control Document, NASA JPL CloudSat project document Version 1.0, 61 pp., 2012.

Wendler, G. and Y. Kodama, 1993: The kernlose winter in Adelie Coast. *Antarctic Meteorology and Climatology: Studies Based on Automatic Weather Stations (eds D. H. Bromwich and C. R. Stearns) American Geophysical Union, Washington, D.C.*, DOI:10.1029/AR061p0139, **61**, 139-147.

Wendler, G., J. C. Andre, P. Pattre, J. Gosink, and T. Parrish, 1993: Katabatic winds in Adelie Coast. *Antarctic Meteorology and Climatology: Studies Based on Automatic Weather Stations (eds D. H. Bromwich and C. R. Stearns) American Geophysical Union, Washington, D.C.*, DOI:10.1029/AR061p0023, **61**, 23-46.

Wood, N. B. and L'Ecuyer, T. S.: Level 2C Snow Profile Process Description and Interface Control Document, Product Version, P1R05, NASA JPL CloudSat project document revision 0, 26 pp., available at: http://www.cloudsat.cira.colostate.edu/sites/default/files/products/files/2C-SNOW-PROFILE_PDICD.P1_R05.rev0_.pdf, last access: 28 June 2018.

Zhu, J., Xie, A., Qin, X., Wang, Y., Xu, B., and Wang, Y., 2021: An assessment of ERA5 reanalysis for Antarctic near-surface air temperature. *Atmos.*, **12**, 217, DOI: 10.3390/atmos12020217.